Rings and Things

David Ormrod Morley
Balliol College
University of Oxford

A thesis submitted for the degree of
Doctor of Philosophy

Trinity 2020

Contents

1 Modelling Bilayer Materials **1**
1.1 Bilayer Materials 1
1.2 Review of Existing Methods 2
1.3 Triangle Raft Method 4
1.3.1 Potential Model 4
1.3.2 Algorithmic Details 5
1.4 Properties of Triangle Rafts 7
1.4.1 Network Growth 8
1.4.2 Network Properties 10
1.4.3 Physical Properties 15
1.5 Chapter Summary 18

2 Persistent Homology for Amorphous Materials **21**
2.1 Introduction to Persistent Homology 21
2.2 Computing Persistent Homology 23
2.2.1 Filtered Simplicial Complexes 23
2.2.2 Homology and Persistent Homology 25
2.2.3 Visualising Persistence 28
2.3 Persistent Homology with Triangle Rafts 31
2.3.1 Overview of Persistence Diagrams 32
2.3.2 Band Structure in Persistence Diagrams 32
2.3.3 Cycles, Betti Numbers and Ring Statistics 39
2.4 Persistent Homology with CRNs 42
2.4.1 Persistence Diagrams 43
2.4.2 Evolution in Betti Numbers 44
2.5 Chapter Summary 44

Appendices

References **49**

List of Notes By David

1 Why again...some inorganic stuff... 2
2 Accompanying figure 5
3 add ellipse appendix 18
4 change **r** in Voronoi chapter 23
5 change all $r_{ij} \to d_{ij}$ 23
6 remake 2.1 consistent with 2.5 24
7 link 29
8 link 31
9 link 31
10 link 31
11 link 42
12 link 42

List of Notes By Mark

1 Have you discussed somewhere why they are doing this? Control of the pore size and pote density critical for gas separation applications.... . . . 2
2 Note somewhere that making the GeO2 analogue is more difficult experimentally..... 2

1 | Modelling Bilayer Materials

A computationally tractable Monte Carlo method using triangle rafts is developed to generate configurations for bilayers of SiO_2 and related materials. The method allows defect free networks of any given shape to be grown with both tuneable ring statistics and topologies, controlled by a combination of the choice of the "allowed" rings and the effective growth "temperature". Configurations are generated with Aboav-Weaire parameters commensurate with those obtained from an analysis of experimental configurations, improving significantly on previous methods for generating these networks (which systematically underestimate this parameter). The ability to efficiently grow configurations allows exploration of the structural basis of Lemaître's law, where the commonly observed value of $p_6 \approx 0.4$ is presented as a balance between entropic and enthalpic contributions to the free energy. The deviations of ring areas from the ideal values are discussed and the relative insensitivity of the ring area to relatively strong distortions is highlighted.

1.1 Bilayer Materials

An important class of two-dimensional materials which have emerged in the 21st century are bilayers of silica, SiO_2, and related species [11]. These can be prepared experimentally by chemical vapour deposition on metal and graphene supports [4, 5]. As in the three-dimensional glass, the basic building blocks of silica bilayers are vertex sharing SiO_4 tetrahedra, maintaining full coordination for all atoms in the bulk [22]. These are arranged such that three of the vertices are connected to tetrahedra in the same layer, with the final vertex being shared between layers acting as a "bridge" (figure 1.1a). A consequence of these bridging oxygen atoms is to enforce a symmetry plane between the upper and lower layers.

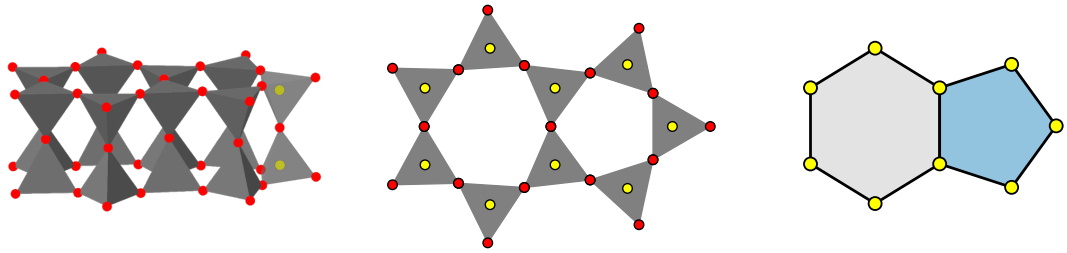

(a) Tetrahedral bilayer **(b)** Triangle raft **(c)** Ring structure

Figure 1.1: Silica bilayers of vertex sharing tetrahedra, (a), can be represented as a two-dimensional triangle raft, (b), (silicon and oxygen atoms are coloured yellow and red respectively). The ring structure then emerges from the three-coordinate network comprising the silicon atoms, (c).

Topologically, the symmetry plane means that these materials can be viewed as effective two-dimensional networks. Taking one of the layers, without the bridging oxygens, and projecting the atoms onto the horizontal plane reveals a representation of vertex sharing triangles, referred to as a triangle raft (figure 1.1b). The ring structure then emerges from the three-coordinate network formed by connecting the silicon atoms of adjacent triangles as in figure 1.1c. Indeed, scanning tunnelling microscopy (STM) has been used to directly visualise the ring structure in silica bilayers, revealing both crystalline and glassy arrangements and even the interface between the two [122, 123].

More recently experimentalists have also succeeded in synthesising bilayers of germania, GeO_2 [7, 8]. These have the same fundamental structure as SiO_2, but with more distorted tetrahedra Why again...some inorganic stuff... . This can lead to a build up of strain and rumpling of the tetrahedral layers. Have you discussed somewhere why they are doing this? Control of the pore size and pote density critical for gas separation applications.... Note somewhere that making the GeO2 analogue is more difficult experimentally.....

1.2 Review of Existing Methods

As mentioned in the introduction, both *ab initio* methods and classical molecular dynamics have been used in computational studies of silica bilayers, which often require a starting atomistic configuration [20–22, 28]. One approach is to simply

take an experimental sample as the starting structure. Whilst this is on the surface the best solution, the experimental configurations may contain defects or areas where the image is corrupted *i.e.* the configuration may not be "pristine". Additionally, the location of each atom has an associated uncertainty which leads to discrepancies in the observed bond lengths and angles, which can be compounded by any out-of-plane distortions. Whilst computational refinement can attenuate these problems [23, 124], there remains the more fundamental question of how "typical" the available images are from experiment, as STM provides exceptional information but only on relatively small sample sizes. Computational techniques can therefore prove a valuable tool for generating a large number of high-quality configurations, and corroborating experimental information.

One current approach is to transform amorphous graphene configurations [22]. Here amorphous samples of carbon are generated using a bond switching method (as outlined in section **??**), before the carbon atoms are swapped from silicon and decorated with oxygens. Whilst this is a valid approach, the method assumes that the two materials are topologically equivalent. This is likely an oversimplification, as the presence of the bridging oxygens in silica afford the structure increased flexibility when compared to the carbon analogue. This likely explains why this method has struggled to mirror experimentally observed values of the ring statistics and Aboav-Weaire parameter, with small and large rings being under-estimated [29].

An alternative approach is to use molecular dynamics coupled with an effective pair potential to obtain viable configurations [28]. Such methods are relatively common, having been employed previously to study amorphous graphene [99]. Such methods offer the potential for generating realistic configurations but are difficult to control as the cooling rates which must be applied are necessarily huge compared to experimental rates. A potential artefact of the high cooling rates is the effectively freezing in of defect states, either in terms of local coordination environments or highly-strained (three-membered) rings. In addition, as with the method above, such methods appears to systematically underestimate the Aboav-Weaire parameter, indicative of too little structural ordering.

1.3 Triangle Raft Method

The motivation of this work was to develop a construction algorithm to generate samples of silica bilayers which can capture the full two-dimensional network topology; both the ring distribution *and* correlations. The model should be able to explore all phases from crystalline to amorphous yet computationally efficient enough to produce configurations suitable for further high throughput calculations. To achieve this a grow-from-seed Monte Carlo algorithm has been developed, where rings are individually added to build a triangle raft. This approach takes inspiration from the first hand-built models, which have been noted to bear good similarity to experimental structures [125, 126]. Such models were superseded by computational techniques designed to generate periodic configurations. However, the recent development in techniques to simulate aperiodic samples, such as sliding boundary conditions for molecular dynamics [127], makes this constraint no longer essential, and benefit may be gained from the added freedom of an aperiodic model.

1.3.1 Potential Model

As explained in figure 1.1 it is possible to capture the full topology of silica bilayers with a simplified representation consisting of a network of vertex-sharing SiO_3 triangles. As the focus of this chapter is on generating a large number of samples with varying ring statistics, to be used as a base for further calculations, working with this reduced representation is sufficient, as it provides a computationally efficient way to produce networks with the required *topology*. The precise *geometry* of the bilayer can be refined with advanced optimisation techniques if required [128].

In order to simulate bilayer systems in two-dimensions, a suitable potential model is needed which captures the essential physics of the system: the local triangular environment of the SiO_3 units and the relative energies of rings of different sizes. The model used here is modified from a relatively simple potential used in all-atom bilayer calculations [22, 23]. Each SiO_3 unit has a harmonic potential acting between

all three Si–O pairs, and the three nearest-neighbour O–O pairs, given by:

$$\mathcal{U}_{ij} = \frac{K}{2}\left(r_{ij} - r_{ij}^0\right)^2, \tag{1.1}$$

where K is a constant, r_{ij} is the interatomic separation and r_{ij}^0 the equilibrium interatomic separation between i, j. The spring constant, k, is set to be very stiff, whilst the equilibrium separations are set according to elemental species such that $r_{\mathrm{OO}}^0 = \sqrt{3}\, r_{\mathrm{SiO}}^0$, maintaining a set of ideal SiO_3 triangles.

The Si–O–Si angle, which determines the strain associated with different ring sizes, is controlled by a shifted and cut 24-12 potential of the form:

$$\mathcal{U}_{ij} = \begin{cases} \epsilon\left[\left(\frac{r_0}{r_{ij}}\right)^{24} - 2\left(\frac{r_0}{r_{ij}}\right)^{12}\right] + \epsilon & r_{ij} \leq r_0 \\ 0 & \text{otherwise} \end{cases} \tag{1.2}$$

where ϵ is a constant and r_{ij} is now the Si–Si separation between atoms in adjacent triangles. It is the value of r_0 which sets the Si–O–Si angle at which strain begins to be felt and therefore the relative ring energies. Taking the hexagonal lattice as being the zero in energy it follows that $r_0 = 2r_{\mathrm{SiO}}$. Rings which deviates increasingly from the ideal hexagon will therefore incur an increasingly energetic penalty.

To summarise, the primary aim here is to generate topologies suitable for later investigation using more detailed (and hence more accurate but more computationally-demanding) potential models. As a result, the harmonic springs simply control the local (triangular) geometries whilst the 24-12 potential controls the repulsion between these local polyhedra. These functions are chosen as deliberately simple to improve computational efficiency and achieve high throughput of idealised networks. Furthermore, the parameters k and ϵ need have no direct physical meaning, simply controlling the meaning of the system "temperature" as discussed below. The only requirement is that they generate energies of the same magnitude to allow for efficient structural evolution. Accompanying figure

1.3.2 Algorithmic Details

Using the model detailed above, a Monte Carlo construction algorithm has been developed which allows two-dimensional networks to be built ring by ring in the shape of a specified function. The main steps of the algorithm are outlined below:

1. Take a starting seed, such as a single ring or experimental configuration
2. Select triangles on which to build the next ring (see figure 1.2)
   (a) Overlay a function on the network (*e.g.* circle, square)
   (b) Check for atoms with dangling bonds lying inside the function region
   (c) If no such atoms exist, systematically increase the function size until an atom is found
   (d) Find the next nearest atoms which also have a dangling bonds
   (e) Choose the two triangles that correspond to the largest starting ring size
3. Determine the probability of constructing rings of different sizes
   (a) Build trial rings in the range k_{min} to k_{max} (see figure 1.3)
   (b) Geometry optimise the local structure and calculate minimised potential energy (as explained in section **??**)
   (c) Calculate the probabilities of each ring occurring, P_k, equation (1.3)
4. Accept single trial ring according to the probability distribution
5. Repeat steps 2 → 4 until the target number of rings is reached

The probability of a ring of size k being accepted, P_k, is given by the equation:

$$P_k = \frac{\exp\left[-\left(\mathcal{U}_k - \mathcal{U}_k\right)/T\right]}{\sum\limits_k \exp\left[-\left(\mathcal{U}_k - \mathcal{U}_0\right)/T\right]}, \tag{1.3}$$

where $\mathcal{U}_k$ and $\mathcal{U}_0$ correspond to the energy of the trial structure and lowest energy of all trial structures respectively, and T is a "temperature". The parameter T controls how easily the potential energy landscape can be explored, and therefore how accessible strained rings become. In the low T limit, the acceptance probabilities are dominated by the energy term, and the rings which are selected will be those with the lowest energy. Note that this is not necessarily the 6-ring, but rather is dependent on the local environment. On the other hand, in the high T limit, the acceptance probabilities are approximately equal, and rings are selected on a more

(a) (b)

Figure 1.2: Panel (a) shows how triangles used to construct a ring are initially selected. There are no atoms with dangling bonds within the first search region (blue dashed line), and so the search area is extended (red dashed line), where triangles A and B are found. Panel (b) gives the three possibilities for the triangles that will form part of the constructed ring: A–C–D–B, A–E, B–F. As A–C–D–B corresponds to the largest starting ring size this is selected.

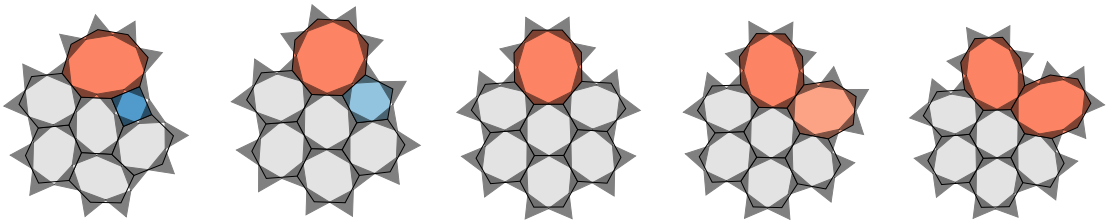

(a) (b) (c) (d) (e)

Figure 1.3: Geometry optimised structures for trial rings in the range $k = 4 - 8$. The ring structure is shown along with the SiO_3 triangle

Table 1.1: Variation of acceptance probabilities with temperature for the configurations in figure 1.3.

P_k	4	5	6	7	8
$T = 10^{-4}$	0.0000	1.0000	0.0000	0.0000	0.0000
$T = 10^{-3}$	0.0000	0.8837	0.1162	0.0001	0.0000
$T = 10^{-2}$	0.0336	0.4104	0.3351	0.1659	0.0550
$T = 10^{-1}$	0.1734	0.2227	0.2183	0.2034	0.1822
$T = 10^{0}$	0.1973	0.2023	0.2018	0.2004	0.1982

random basis. This is demonstrated in table 1.1, using the example configurations from figure 1.3. The "temperature" parameter is therefore the primary method for controlling the distribution of ring sizes in constructed networks.

1.4 Properties of Triangle Rafts

The triangle raft method is evaluated in terms of its effectiveness in producing configurations which accurately replicate the network properties of experimental

silica bilayers *i.e.* the ring statistics and Aboav-Weaire parameter. It is also compared against the existing methods introduced in section 1.2, namely generation from amorphous graphene or molecular dynamics. This is performed in wider context of systematically varying the model parameters to explore the behaviour of generic networks of this type.

1.4.1 Network Growth

The triangle raft method is robust and controllable, and is able to generate configurations with tuneable ring statistics and topologies. Results will largely focus on the system where $k = 4 - 10$, denoted $\{4, 10\}$, mimicking the experimentally observed range for silica bilayers. Six example configurations are given in figure 1.4, which are generated with a range of temperatures and growth geometries. Figures 1.4a-1.4d provide a good qualitative analysis of the effect of temperature on the ring structure. At low temperature a phase boundary can be seen separating crystalline and amorphous regions, as seen in experimental silica bilayers [123]. In these samples although the proportion of small and large rings is low, their positions are highly correlated and chain structures of alternating rings sizes are clearly present. These motifs are reminiscent of defects found in a wide range of materials, including amorphous graphene and thin silicon and germanium oxides [3, 7, 11, 20]. The increase in temperature is coupled with the emergence of rings of more extreme sizes and regions which could be viewed as nano-crystalline are dispersed. The high temperature limit reveals a fully amorphous structure.

Figures 1.4e and 1.4f give examples of the diverse geometries in which samples may be constructed. It is interesting to note that even "difficult" shapes, such as those containing concave regions and cusps, do not prevent growth. Although the shape does not affect the network topology and is in a sense arbitrary, certain calculations may benefit from the different configurational shapes. For instance, molecular dynamics with sliding boundary conditions requires fitting of a smooth function to the sample perimeter, which is facilitated by having a near-circular form. Other areas such as percolation problems may benefit from square samples.

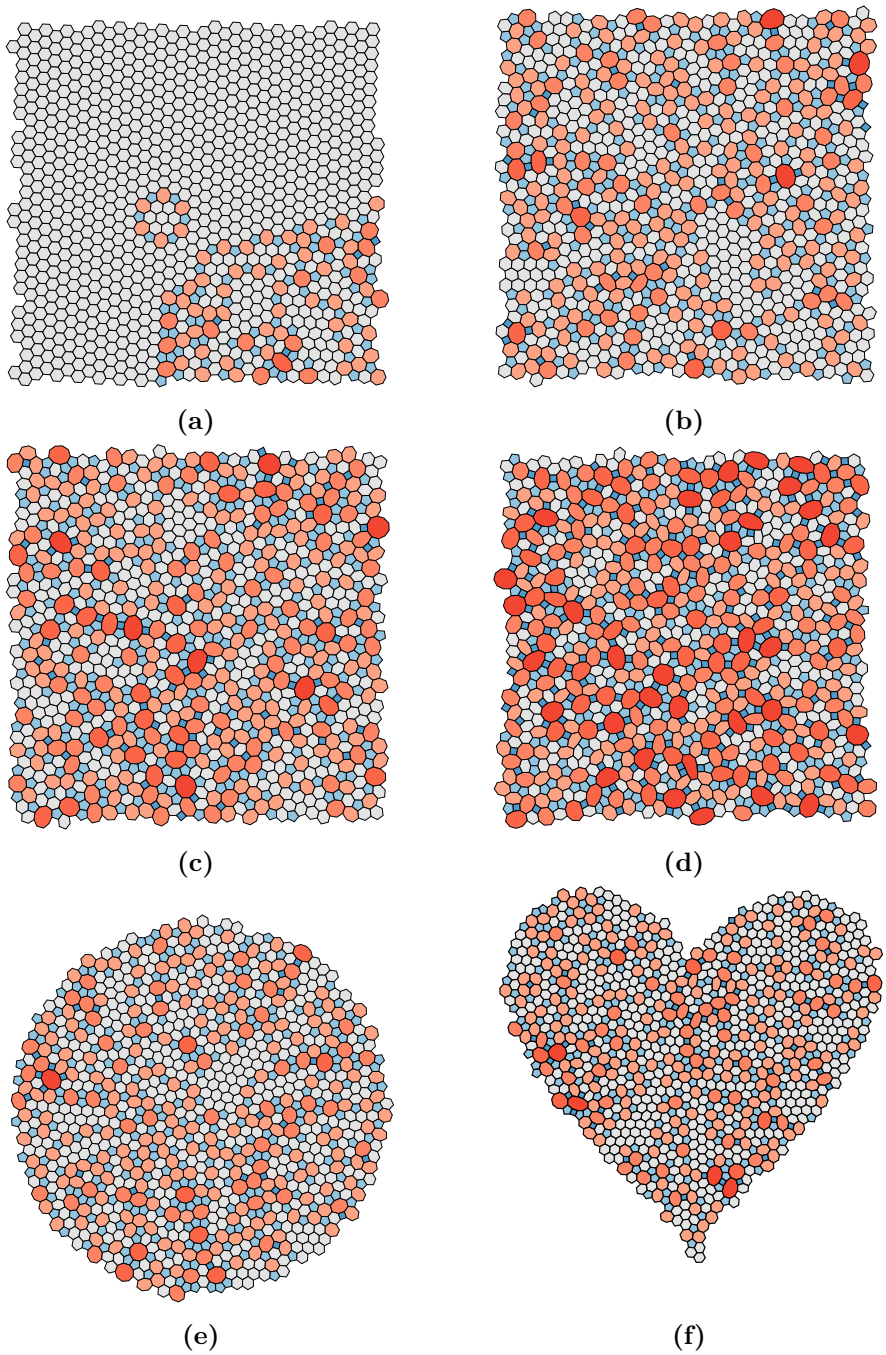

Figure 1.4: Example 1,000 ring configurations generated with different temperatures and shapes. Panels (a) through (d) show square lattices grown at $T = 10^{-4.0}$, $10^{-3.0}$, $10^{-2.5}$, $10^{-2.0}$ respectively. The samples show the increasing diversity in ring structure as temperature is increased. Panels (e), (f) show configurations with alternative lattice shapes at $T = 10^{-3.0}$, demonstrating the flexibility of the method in growing samples with variable geometries. Rings are coloured according to size with $k < 6$ as blue, $k = 6$ as grey and $k > 6$ as red.

1.4.2 Network Properties

The quantitative relationship between temperature and ring structure was investigated for three systems of varying ring size ranges; $\{5,7\}$, $\{4,8\}$ and $\{4,10\}$. For each system, 100 samples consisting of 1000 rings were grown at temperatures between $T = 10^{-4.5} \rightarrow 10^{-1.5}$. The evolution of the combined ring statistics with temperature is presented in figure 1.5. Figures 1.5a-1.5c give bar representations of the ring size distributions for the three systems, which show different behaviours. For $\{5,7\}$ the individual p_k are all monotonically increasing ($k \neq 6$) or decreasing ($k = 6$) functions, but both $\{4,8\}$ and $\{4,10\}$ have p_k containing maxima. Additionally, both $\{5,7\}$ and $\{4,8\}$ achieve uniform distributions in the high temperature limit but $\{4,10\}$ does not.

This disparity in behaviour can largely be traced back to the constraint of Euler's theorem. As $\{5,7\}$ comprises of just three ring sizes, Euler's formula demands that $p_5 = p_7 = (1 - p_6)/2$ and so the system is relatively well defined. Hence as the 5 and 7-rings are more strained than the 6-ring, p_5 and p_7 show a systematic increase with temperature. Furthermore, the uniform equilibrium distribution can only satisfy Euler's formula when the ring size range is symmetric about 6, as is observed for $\{5,7\}$ and $\{4,8\}$. The form of the ring statistics at intermediate temperatures and for $\{4,10\}$ follow the maximum entropy solutions according to Lemaître's law, discussed in section **??** and later in this section.

The ring distribution for $\{4,10\}$ is also shown as a function of temperature in figure 1.5d, along with the value of the Aboav-Weaire parameter, α, allowing for more facile comparison with experiment. The temperature which gives the best agreement between our model and amorphous experimental samples is highlighted by the vertical dashed line. The values of p_k and α are provided in table 1.2, alongside results from two experimental samples. It is evident that the model can be successfully tuned to match the topology of the experimental system. Not only are the ring distributions in very good accordance, but also the ring correlations, which have until now proved difficult to capture. This provides confidence that

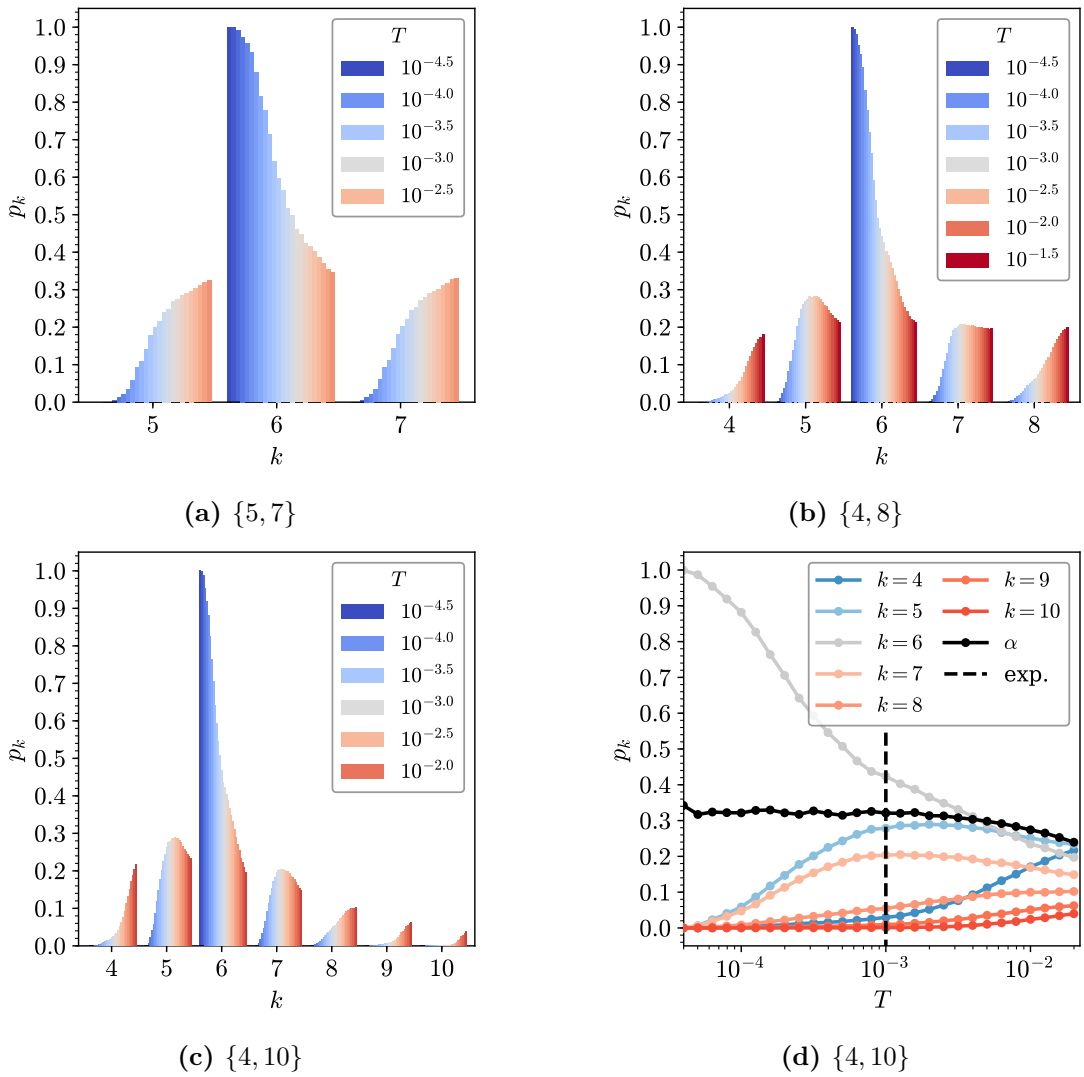

(a) $\{5, 7\}$ **(b)** $\{4, 8\}$

(c) $\{4, 10\}$ **(d)** $\{4, 10\}$

Figure 1.5: Variation in ring statistics with temperature over a given allowable k-range. Panels (a)-(c) show bar graph representations of the ring statistics, coloured by temperature, for the $\{5, 7\}$, $\{4, 8\}$ and $\{4, 10\}$ systems, respectively. Panel (d) gives an alternative line graph representation of the ring statistics for $\{4, 10\}$, coloured by ring size, along with the Aboav-Weaire parameter. The temperature which gives the best match to the experimentally observed amorphous region is also highlighted (vertical black dashed line).

this simplified but physically motivated triangle raft model is able to reproduce the behaviour of real systems.

Table 1.2: Comparison of silica bilayer samples from experiment, computational modelling and theory.

	Experiment		Computation				Theory
	Ru(0001) [126]	Graphene [4]	MC[a] [29]	MC[a] [29]	MD[b] [28]	TR[c]	Lemaître [57]
$\mathcal{N}$	317	444	216	418	16×85000	1000×100	–
p_3	0.0000	0.0000	0.00	0.00	0.0038	0.0000	0.0000
p_4	0.0379	0.0383	0.02	0.00	0.0537	0.0295	0.0280
p_5	0.2744	0.2725	0.33	0.37	0.2686	0.2786	0.2834
p_6	0.4448	0.4189	0.37	0.32	0.3773	0.4234	0.4200
p_7	0.1609	0.2117	0.21	0.25	0.2224	0.2034	0.2077
p_8	0.0757	0.0495	0.07	0.06	0.0602	0.0544	0.0518
p_9	0.0063	0.0068	<0.01	0.00	0.0118	0.0097	0.0082
p_{10}	0.0000	0.0023	0.00	0.00	0.0018	0.0010	0.0009
$p_{>10}$	0.0000	0.0000	0.00	0.00	0.0004	0.0000	0.0000
μ_2	0.9460	0.9333	0.94	0.86	1.1302	0.9208	0.8985
α	0.32	0.33	0.18	0.23	0.25	0.32	–

Note: Each method is given alongside the number of rings in the sample, $\mathcal{N}$, followed by the ring statistics, p_k, the second moment of the ring statistics, μ_2, and the Aboav-Weaire parameter, α
[a] Bond Switching Monte Carlo (graphene potential) [b] Molecular Dynamics
[c] Triangle Rafts, this work, $T = 10^{-3}$

Table 1.2 also lists the ring statistics obtained from previous computational studies which used both Monte Carlo and molecular dynamics methods. As mentioned in the review of these methods above, neither fully succeeds in accurately capturing the topology of silica bilayers. Kumar *et al.* attempted to transform an amorphous graphene structure generated from bond switching Monte Carlo into a silica bilayer. The ring statistics of the resulting structure were approximately correct, but the proportion of 5- and 6- rings over- and under-estimated respectively. In addition the Aboav-Weaire parameter was substantially lower than experiment, indicating a relative lack of structure in the ring ordering. The origin of these discrepancies is likely the use of a graphene potential model. The increased stiffness of the carbon network (which unlike silica lacks bridging oxygens) means a high temperature must be used to obtain an amorphous structure with the required disorder. This leads to heavily distorted rings (as noted in the original paper) which reduces the requirement for small rings to be adjacent to large.

Roy *et al.* have an alternative approach of generating configurations with an effective pair potential and molecular dynamics. As can be seen the ring statistics are closer to the experimental values, but now contain artefacts, with a significant fraction of highly strained 3-membered rings and large rings up to $k = 14$. These manifest as a result of the artificially high cooling rates in the computational studies which trap defect states in the configurations. Once again the final Aboav-Weaire parameter, α, is underestimated.

It is worth re-emphasising here that the triangle raft method is able to replicate experimental values of both p_k and α, due to its tuneable approach and "organic" growth mechanism, where sample formation is not influenced by enforced periodicity. Beyond this, the controllable nature of the method also allows insight into key questions about silica bilayers, for instance the form of the ring distribution in this amorphous phase. As detailed in section **??**, the maximum entropy ring distribution can be calculated numerically given the value of p_6. For example, table 1.2 gives the maximum entropy solution for $p_6 = 0.42$, which agrees very well with the results from

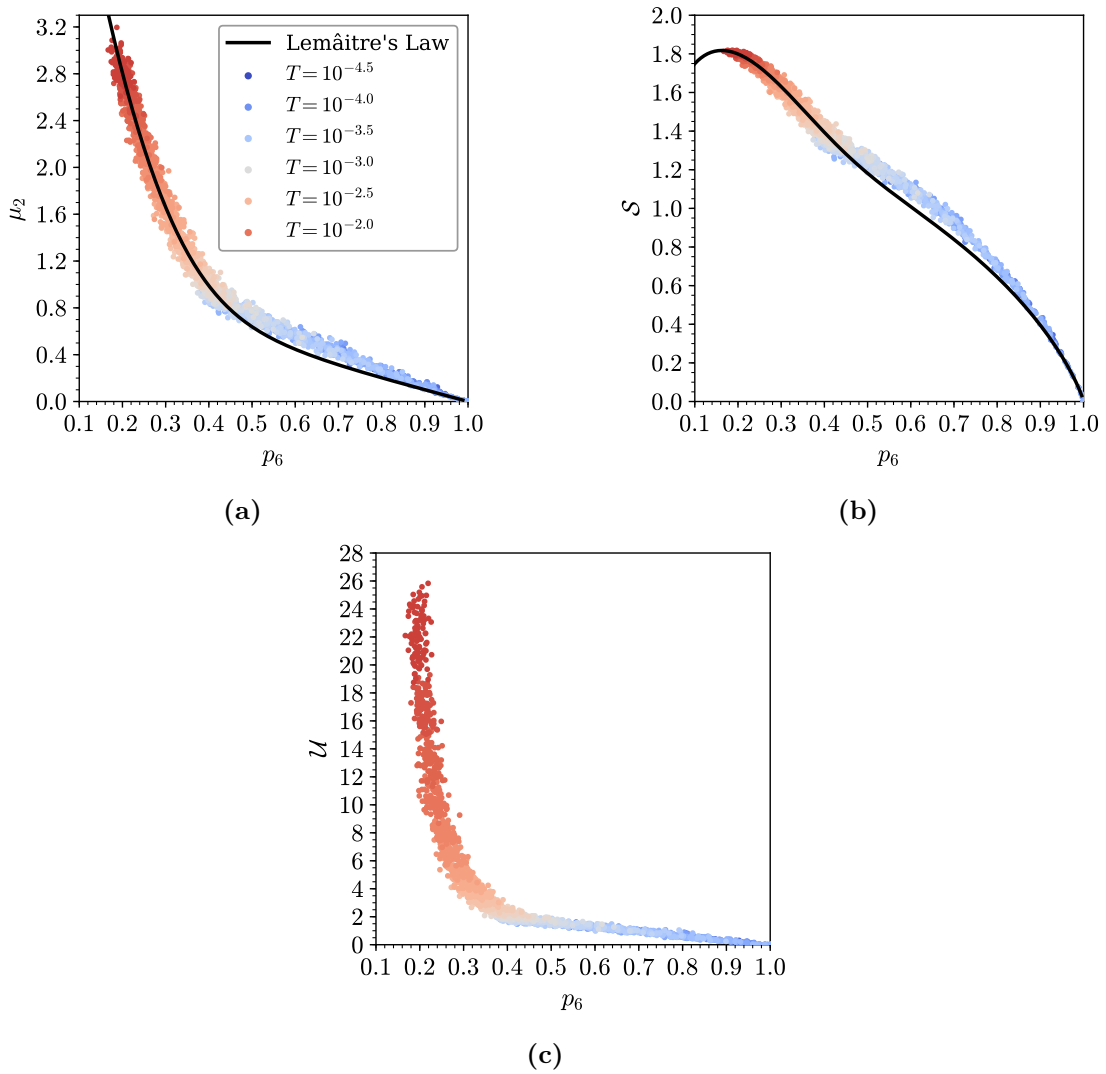

Figure 1.6: Evolution of ring statistics (a), entropy (b) and potential energy (c) of triangle rafts with temperature. The experimental value of $p_6 \approx 0.4$ occurs just before the exponential increase in potential energy, reflecting the balance of energetic and entropic factors.

triangle rafts and experiment. This second moment of the distribution, μ_2, is then uniquely related to p_6 via Lemaître's law, shown as the black line in in figure 1.6a.

However, Lemaître's law gives no information on why a particular maximum entropy distribution is found for a given system. The triangle raft method allows systematic generation of configurations with different p_6 values by tuning the temperature parameter. The resulting configurations follow Lemaître's law across the entire temperature range. Figures 1.6 gives the results from the individual 1000 ring samples, coloured by temperature. Figures 1.6a and 1.6b compare the

observed μ_2 and S (entropy) of the generated configurations to those expected from Lemaître's law, showing the law provides a good fit, with only a small deviation observed for $p_k > 0.5$.

Figure 1.6c plots the geometry optimised potential energy of the samples against p_6, which increases as the ring sizes become more diverse. The curve is split into two regimes, with gradual increase in energy from $p_6 = 1.0 \rightarrow 0.4$ followed by exponential increase for $p_6 < 0.4$. This is consistent with the information in figure 1.5d which shows that below $p_6 \approx 0.4$, not only does the number of extreme ring sizes increase rapidly, but they become less correlated with a lower α, decreasing the number of favourable small-large ring pairings.

It can now be proposed why the experimental amorphous distributions are found with a value of $p_6 \approx 0.4$. The system aims to maximise entropy by obtaining a ring distribution along the Lemaître curve with the minimum p_6 possible. However, for $p_6 < 0.4$ the energetic cost becomes prohibitively large, as higher entropy distributions can only be achieved by increasing the proportion of extreme ring sizes at the expense of relatively low strain 5- and 7- rings. Interestingly it is also evident why no configurations are present below $p_6 \approx 0.16$, even at the highest temperature. Below this point, the entropy of the $\{4, 10\}$ system decreases whilst the energy continues to rise and so there is no driving force to sample this area of phase space.

1.4.3 Physical Properties

As an additional check that the developed triangle raft model behaves physically, the angle distribution between adjacent SiO_3 units, $f(\theta)$, was calculated for the $\{4, 10\}$ system across the range of temperatures studied. The results are summarised in figure 1.7a. The angle distributions are necessarily symmetric about 120°, as each triangle pair contributes two complementary angles. At lower temperatures the distribution is dominated by angles close to 120°, as a consequence of the large proportion of near strainless six membered rings. Furthermore, at the temperature corresponding to the amorphous experimental region, $T = 10^{-3}$, the distribution has a similar extent to the angle distribution found in experimental samples (see

for example figure 7 reference [28]). However, as the temperature increases, the form of $f(\theta)$ does not simply broaden as might be expected, but becomes bimodal. This can be rationalised by considering the angles that would be present in regular polygons of different sizes, marked by vertical lines in figure 1.7a. These ideal angles are clustered away from the mean value of 120°, and hence increasing the diversity of ring sizes through temperature acts to shift the most commonly observed angles from the central value of 120°. It is therefore interesting to note that increasing structure in the angle distribution does not necessarily translate to increased order in the atomic configurations.

A final check comes from examining the ring areas in the generated configurations. Inspection of amorphous experimental samples reveals that the rings appear highly regular in shape. This can be quantified by determining the average dimensionless area for each ring size, A_k, and comparing it to the area of the corresponding regular polygon, A_k^0, where:

$$A_k = \frac{\langle Area\,(k)\rangle}{\left(r^0_{\mathrm{SiSi}}\right)^2}, \tag{1.4}$$

$$A_k^0 = \frac{k}{4\tan\left(\pi/k\right)}. \tag{1.5}$$

As the regular polygon has the maximum achievable area for a given ring size, the ratio A_k/A_k^0 is expected to lie in the range $0 \to 1$, with a lower value corresponding to increased deviation from regularity, and assuming r^0_{SiSi} to be fixed.

The study by Kumar *et al.* found that whereas for experimental configurations, $A_k/A_k^0 \approx 1$, configurations generated using thier bond switching method generally displayed ratios much less than unity [99], indicative of large distortions in the ring structure. For larger rings, a value of $A_k/A_k^0 > 1$ was also found, which can only be achieved if there is appreciable bond stretching (see equations (1.4), (1.5)).

The analogous results for the method presented in this chapter can be found in figure 1.7b, for $T = 10^{-3}$. This figure demonstrates that there is now good agreement between experimental and computational results. In both cases the deviation from regularity increases with ring size, as the flexibility of the rings

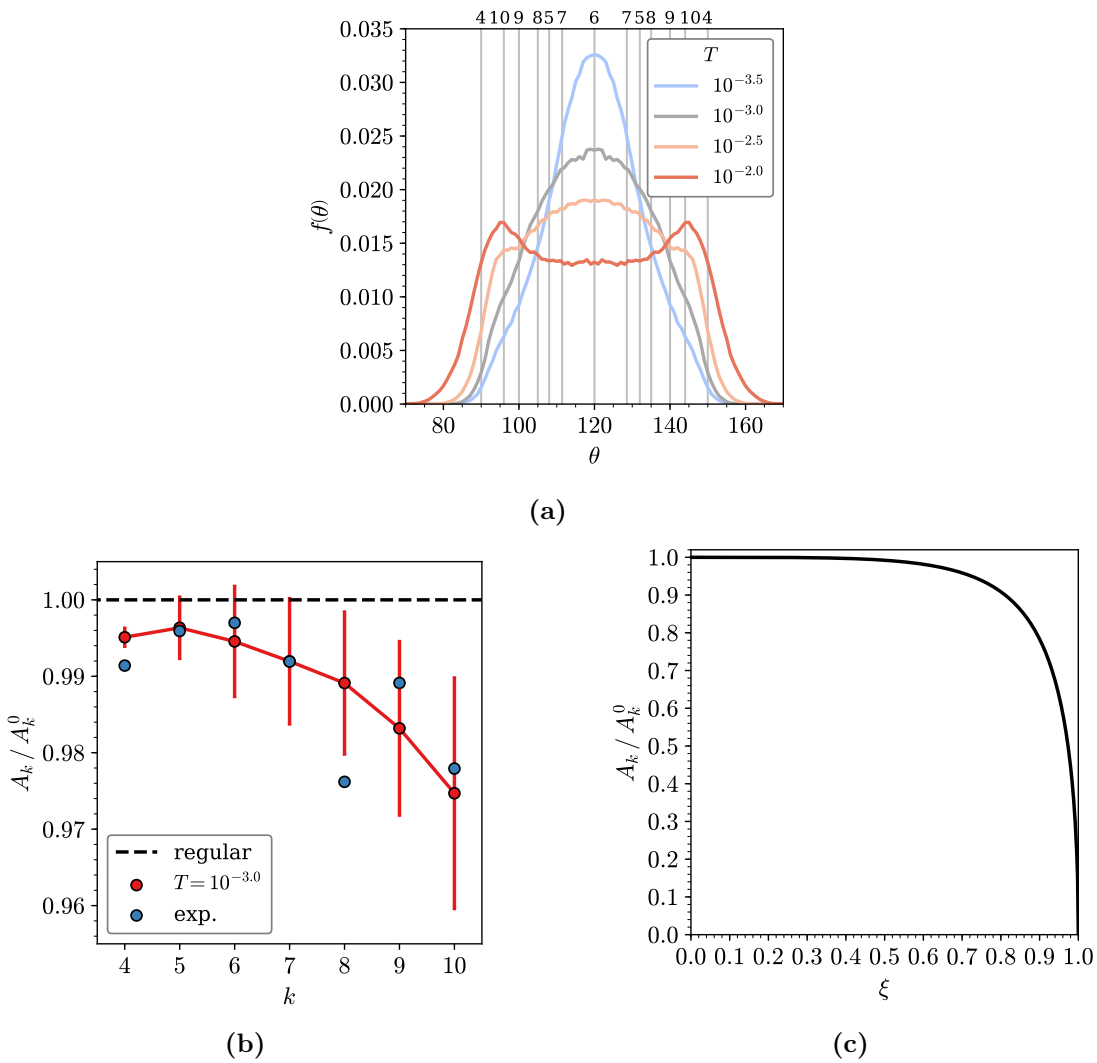

Figure 1.7: Panel (a) gives the ring angle distribution function for triangle rafts formed at different temperatures. Panel (b) compares the regularity of rings in computational and experimental amorphous configurations, with points indicating the mean value and bars corresponding to the standard deviation. Experimental data is taken from ref. [29]. Panel (c) shows the effect on the area when distorting a circle to an ellipse whilst maintaining a constant perimeter length.

increases. Again it can be proposed that the difference between current and previous methods could be due to the lack of enforced periodicity on the system. By allowing the network to grow relatively freely, the system can avoid a build up of strain associated with maintaining periodic boundaries.

Even with this analysis, an argument can be made that by visual inspection the rings in the experimental configurations are still more regular than those generated from computational samples. Therefore one can consider if deformation of a ring

should be expected to lead to significant reduction in area. This can be explored by considering the distortion of a circle to an ellipse. The degree of distortion can be described by the eccentricity of the ellipse,

$$\xi = \left(1 - \frac{b^2}{a^2}\right)^{1/2}, \tag{1.6}$$

where a, b are the major and minor axis radii respectively. This change in area with distortion is shown in figure 1.7c, the calculation of which can be found in appendix add ellipse appendix . As can be seen, a large degree of eccentricity is needed for a significant change in the observable area. For example, if $a = 1.5b$, the area is still $\approx 0.94\%$ of the area of the corresponding circle.

For silica networks the Si–Si distances lie in a narrow range because of the covalent nature of the atomic bonding and the near-linear Si-O-Si bridges which join the two layers. Hence we would expect similar behaviour to occur, with ring areas relatively invariant to distortions in the ring shape (this same analysis would not be expected to hold for foams for example, where the length of the boundary is much more flexible). This suggests that the ring area is not the most suitable metric for quantifying the regularity of rings in systems such as this, and could explain any disagreement between the seemingly near ideal ring areas and the visual evidence. As previously stated, although the potential model used is physically motivated, it is lightweight in order to facilitate generation of a large number of configurations with the correct network topology. In future it would be informative to see if the required regularity can be achieved by geometry optimising the resulting bilayer configurations with a more accurate potential, such as the TS potential which includes potentially significant electrostatic interactions including many-body polarisation effects [128].

1.5 Chapter Summary

In this chapter a method for the effective growth of two-dimensional networks from a given seed has been developed, allowing for control over the ring size distributions

and the system topologies. The latter is often characterised by the Aboav-Weaire parameter, α, and the values obtained here are more commensurate with those obtained from experimental imaging compared with previously constructed configurations. The high throughput method has allowed a detailed analysis of Lemaître's law and has highlighted why the fraction of six-membered rings observed in real systems is often $\sim$0.4. Finally, a consideration of the ring areas show our configurations to contain more regular polyhedra than a number of previous configurations. However, the area itself is shown to be a relatively poor measure of a deviation from ideality for systems of this type.

2 | Persistent Homology for Amorphous Materials

Persistent homology is a technique in topological data analysis to find the fundamental topological features in a collection of points. The applicability of persistent homology to the analysis of network materials is explored here for the relatively simple case of two-dimensional networks. Analysis is carried out for two systems, triangle rafts and CRNs. The persistence diagrams of triangle rafts are shown to have a band structure which originates in successive nearest-neighbour interactions, whilst the evolution of Betti numbers is related to the underlying ring statistics. XXX

2.1 Introduction to Persistent Homology

The need for efficient methods to find structure in large and complex data sets is ever increasing in the age of "big data". The field of topological data analysis (TDA) has emerged to address this need, driving the development of statistical tools to analyse and understand big, noisy, real-world data [222]. One tool in particular has received significant attention, namely that of persistent homology [223]. Persistent homology is concerned with finding the fundamental topological features of given set of points. In slightly plainer terms, here *homology* means counting the number of connected components ("blobs") and cycles ("holes") in a system. The persistence aspect arises from the fact that the these topological features can be calculated across different length scales, with those existing across multiple length scales being identified as more *persistent*. The more persistent a topological feature, the more it can be thought of as reflecting the true underlying system topology.

As with any new technique which arrives with much fanfare, persistent homology has been quickly appropriated for the study of chemical and physical systems. In fact, the marriage of persistent homology and atomistic materials seems apt. Atomic systems have long been thought of in terms of collections of point like particles, and the study of the emergent structure is deep-rooted in the field. Any process which can elucidate as yet hidden structure in materials, or improve its description naturally has potential to be extremely useful. In this vein, research has already been conducted on applying persistent homology to diverse topics such as colloidal packings, porous media, water networks, fullerenes [**Robins2017**, 224–227], and of particular importance to this work, amorphous materials [228–231]. Whilst these latter studies claim to highlight structures which are not available using more conventional techniques, quantify the medium range order in glasses, and explain phenomena such as the origin of the first sharp diffraction peak in disordered materials; the fact remains that persistent homology remains a qualitative descriptor, with some doubt as to what is the "added value" from this technique. In the words of Wassserman: "*...the main purpose of TDA is to help the data analyst summarize and visualize complex datasets. Whether or not TDA can be used to make scientific discoveries is still unclear.*" [222].

The purpose of this chapter is therefore to try and assess the utility of persistent homology in the context of two-dimensional amorphous materials, with the expectation that the interpretation may be simpler for these reduced dimensionality systems. The conclusions drawn from this work may then bring insight to the analysis of three dimensional systems. This chapter will begin by outlining the relevant theory to persistent homology, with the aid of small example systems. Persistent homology will then be calculated for triangle rafts (a proxy for amorphous silica), systematically generated with increasing levels of disorder. These results will then be contrasted with generic random networks as produced from bond switching. Conclusions XXX

2.2 Computing Persistent Homology

This section will give a broad outline of the mathematical background behind persistent homology, but with the focus on a practicable implementation for studying physical two-dimensional networks. It will begin by introducing the concept of a filtered simplicial complex, before discussing homology groups, persistent homology and the visualisation of persistence. Actual numerical persistent homology calculations can be carried out with the GUDHI library [232].

2.2.1 Filtered Simplicial Complexes

The input for a persistent homology calculation is simply a point cloud *i.e.* a set of coordinates in Euclidean space. change $\mathbf{r}$ in Voronoi chapter . change all $r_{ij} \rightarrow d_{ij}$. For materials, this corresponds to the set of atomic positions, $\mathbf{r} = \{r_1, r_2, \cdots, r_{\mathcal{N}}\}$, as obtained from simulation or for instance experimentally via STM. Using this point cloud, a filtered simplicial complex can be constructed [233]. To explain what is meant by a filtered simplicial complex, it is useful to break down this definition further:

- An m-simplex, σ, is a subset of the total points, $\sigma \subseteq \mathbf{r}$, with dimension $m = |\sigma| - 1$. Put simply, a 0-simplex corresponds to a point, a 1-simplex to a line, a 2-simplex a triangle, a 3-simplex a tetrahedron, and so on.

- A simplicial complex, $\mathbf{K}$, is then a set of simplices, $\mathbf{K} = \{\sigma_1, \sigma_2, \dots\}$.

- A filtration of a simplicial complex, is a sequence of subcomplexes: $\mathbf{K}_a \subseteq \mathbf{K}_b \subseteq \cdots \subseteq \mathbf{K}$, where each subcomplex, $\mathbf{K}_\epsilon$, occurs at an increasing filtration value, denoted ϵ (see below).

For a given point cloud, there are many ways to then construct a filtered simplicial complex (Cech, Vietoris-Rips, Witness *etc.*), each method identifying simplices and calculating filtration values in a different manner [234]. In this thesis, for reasons which will become apparent, the *alpha complex* is used.

As an illustration of these concepts, an introductory example with just three points is given in figure 2.1. Considering only the simplices at first: figure 2.1a contains three 0-simplices, the points A, B, C; figures 2.1b and 2.1c three 1-simplices, the lines AB, AC, BC; figure 2.1d a 2-simplex, the triangle ABC. Once the simplices have been identified, a filtration value, ϵ, is computed and assigned to each. For the alpha complex, filtration values are determined from the radius of the circumcircles containing the simplices. The specific algorithm is as follows:

- 0-simplices: must have a filtration value of $\epsilon = 0$.
- 1-simplices: provided the circumcircle is empty, they have a filtration value equal to its radius, which for two points is equivalent to half the line length $\epsilon = d_{ij}/2$. If the circumcircle contains a 2-simplex, then the filtration value is set to the filtration value of that simplex.
- 2-simplices: have a filtration value equal to the circumradius of the three points.

These different cases are shown and explained in figure 2.1.

Having calculated the filtration values for each simplex, a subcomplex can be generated, $\mathbf{K}_\epsilon$, which contains only the simplices with filtration values less than or equal to ϵ. Finally, the filtered simplicial complex emerges as a sequence of subcomplexes at increasing filtration values from $\epsilon = 0 \to \infty$. Again figure 2.1 shows this process for the case of three points. The first subcomplex, $\mathbf{K}_0$, will only consist of a set of discrete points (as in figure 2.1a). As the filtration value increases, higher dimensionality simplices will be included, as lines and triangles form (as in figure 2.1b). The last subcomplex, $\mathbf{K}_\infty$, will contain all the determined simplices (as in figure 2.1d). Crucially, for the alpha complex, this will be equivalent to the Delaunay triangulation. This is the motivation for choosing the alpha complex, as the Delaunay triangulation (which has already appeared throughout this thesis as the dual of the Voronoi diagram), is well defined in two dimensions. As such it provides the best opportunity to relate the results of persistent homology to well understood systems.

remake 2.1 consistent with 2.5

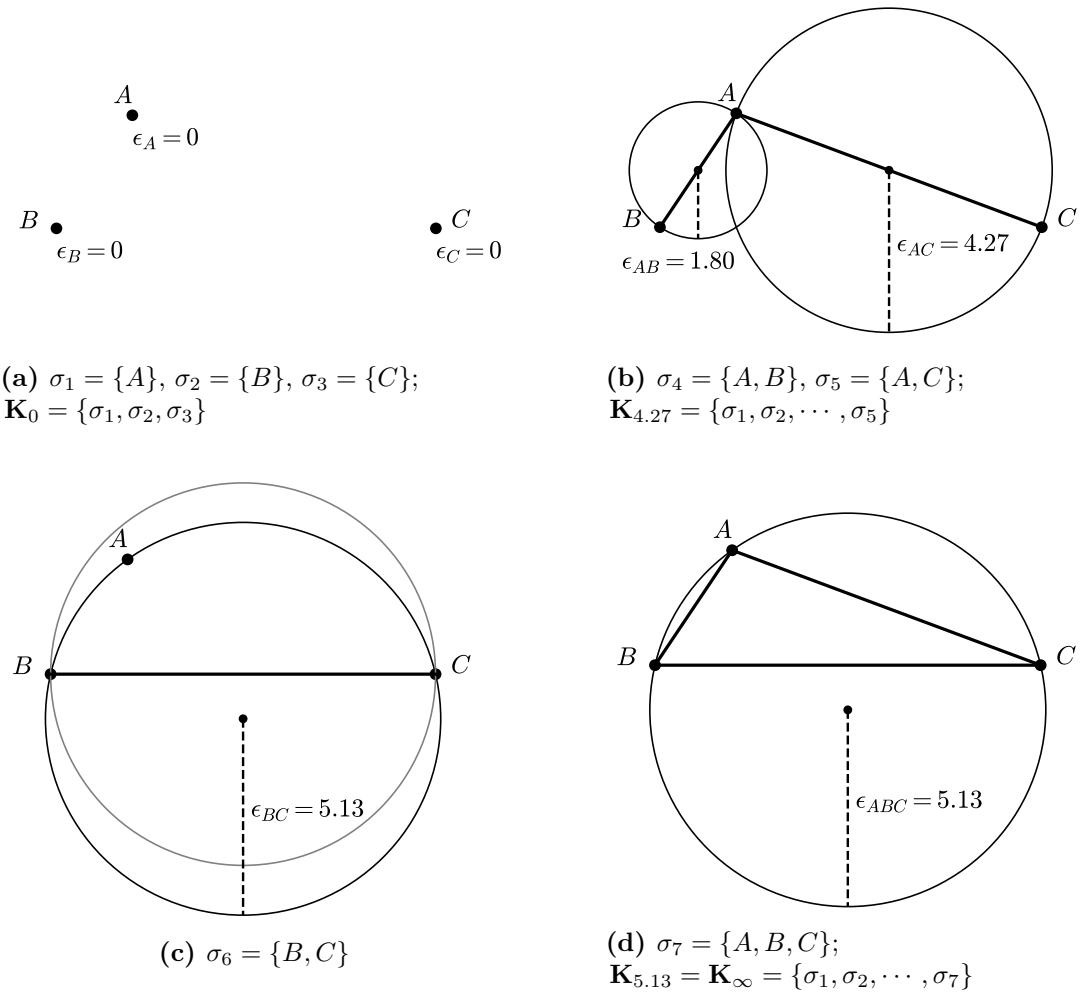

(a) $\sigma_1 = \{A\}$, $\sigma_2 = \{B\}$, $\sigma_3 = \{C\}$; $\mathbf{K}_0 = \{\sigma_1, \sigma_2, \sigma_3\}$

(b) $\sigma_4 = \{A, B\}$, $\sigma_5 = \{A, C\}$; $\mathbf{K}_{4.27} = \{\sigma_1, \sigma_2, \cdots, \sigma_5\}$

(c) $\sigma_6 = \{B, C\}$

(d) $\sigma_7 = \{A, B, C\}$; $\mathbf{K}_{5.13} = \mathbf{K}_\infty = \{\sigma_1, \sigma_2, \cdots, \sigma_7\}$

Figure 2.1: Construction of an alpha simplicial complex and its filtration. Panel (a) shows three 0-simplices, with filtration values of $\epsilon = 0$. Panel (b) shows an additional two 1-simplices, with filtration values given by the radii of the respective circumcircles (dashed lines in black circles). Panel (c) shows an additional different 1-simplex, in which the circumcircle (grey circle) contains the 3-simplex $\{A, B, C\}$, and so the filtration value is set to the value of the 3-simplex. Panel (d) shows an additional 3-simplex with a filtration value given by the circumradius. These subfigures can also be viewed as a series of subcomplexes, as highlighted in the captions, with $\mathbf{K}_0 \subseteq \mathbf{K}_{4.27} \subseteq \mathbf{K}_{5.13} = \mathbf{K}_\infty$. The final complex is the Delaunay triangulation of the original point set. Panel (c) is *not* a subcomplex in the filtration, as it does not contain the simplices $\{A, B\}$, $\{A, C\}$, which have lower filtration values than $\{B, C\}$.

2.2.2 Homology and Persistent Homology

Having introduced the notion of a filtered simplicial complex, the importance of homology and persistent homology can now be discussed. To facilitate this, two more involved examples will be used. Figures 2.2a-2.2d and 2.2e-2.2h show filtrations of alpha complexes for a crystalline and amorphous atomic configuration

respectively, which will be referred to throughout this section.

In this context, homology is generally concerned with quantifying the number of n-dimensional topological features in a simplicial complex. For an alpha complex, these can either be 0- or 1-dimensional. The 0-dimensional features correspond to the number of connected components, meaning the number of distinct groups of atoms. The 1-dimensional features are the number of "cycles" (or "holes") in the structure. These are termed as such to differentiate from "rings" used elsewhere in this thesis, but often there will be significant overlap between the two. Any alpha complex has the homology groups, $H_n(\mathbf{K}_\epsilon)$, which contain all the associated n-dimensional features. The rank of these groups are termed the Betti numbers, β_n [235]. To make this less abstract, one can see how this fits with the examples in figure 2.2:

- Figures 2.2a and 2.2e have $\mathcal{N} = 68$ and $\mathcal{N} = 70$ individual points respectively, and so have Betti numbers of $\beta_0 = \mathcal{N}$ and $\beta_1 = 0$.
- Figures 2.2b and 2.2f have all the atoms connected leading to the formation of 24 cycles in both cases, and hence $\beta_0 = 1$ and $\beta_1 = 24$.
- Figures 2.2c and 2.2g both have a reduced number of cycles owing to the filtration values of triangular simplices being met. The Betti numbers are $\beta_0 = 1$, $\beta_1 = 12$ and $\beta_0 = 1$, $\beta_1 = 10$ in each case.
- Figures 2.2d and 2.2h have just one large connected component and no cycles, such that $\beta_0 = 1$ and $\beta_1 = 0$.

These examples illustrate a more general principle, that the "starting point", $\mathbf{K}_0$, will always have $\beta_0 = \mathcal{N}$ and $\beta_1 = 0$, and the "end point", $\mathbf{K}_1$, will always have $\beta_0 = 1$ and $\beta_1 = 0$ *i.e.* trivial homology. It is the filtration values in between which lead to richer behaviour.

This leads onto the notion of persistent homology. Between any two subcomplexes at different filtration values, a selection of topological features will be common to both, whilst others will appear or disappear when moving from one to the other. In other words, some features will *persist* over the range of filtration values, whilst

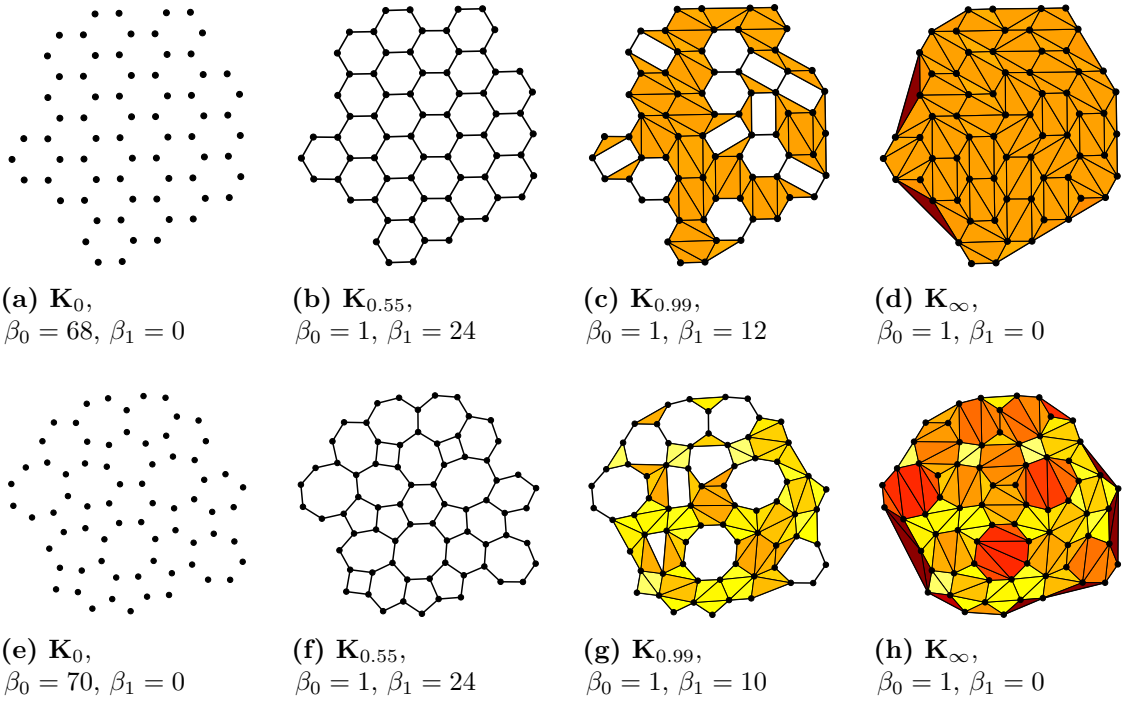

(a) $\mathbf{K}_0$, $\beta_0 = 68$, $\beta_1 = 0$ **(b)** $\mathbf{K}_{0.55}$, $\beta_0 = 1$, $\beta_1 = 24$ **(c)** $\mathbf{K}_{0.99}$, $\beta_0 = 1$, $\beta_1 = 12$ **(d)** $\mathbf{K}_\infty$, $\beta_0 = 1$, $\beta_1 = 0$

(e) $\mathbf{K}_0$, $\beta_0 = 70$, $\beta_1 = 0$ **(f)** $\mathbf{K}_{0.55}$, $\beta_0 = 1$, $\beta_1 = 24$ **(g)** $\mathbf{K}_{0.99}$, $\beta_0 = 1$, $\beta_1 = 10$ **(h)** $\mathbf{K}_\infty$, $\beta_0 = 1$, $\beta_1 = 0$

Figure 2.2: Filtered alpha complexes for a crystalline (a)-(d) and amorphous (e)-(h) configurations. The Betti numbers for the 0- and 1-dimensional features are also given in the captions, corresponding to the number of connected components and cycles respectively. In addition 2-simplices are coloured according to their filtration value, with yellow→red indicating a larger filtration value. This highlights that all 2-simplices form almost simultaneously in the crystalline case, resulting in the death of all cycles, whilst in the amorphous case the formation is more gradual such that larger cycles tend to persist longer.

others will not. To characterise this behaviour in the vocabulary of persistent homology, each feature is said to be "born" at a given filtration value, b, and "die" at a later value, d. The lifetime, or persistence, of the feature is then quantified via $l = d - b$. Finding and measuring the lifetimes of topological features is therefore the crux of persistent homology. In the first instance, it is the longest lived features which are normally of most interest, as these are considered to be representative of the true system topology. In the case of two-dimensional atomic materials, this ought to be reflective of the ring structure. However, other more fleeting features can also be useful, as these intermediate features act as signatures for some medium range ordering [229, 230].

2.2.3 Visualising Persistence

After running a persistent homology calculation by generating a filtered simplicial complex, finding the topological features and determining the lifetimes of each, the results still have to be presented in a way that highlights the fundamental features and facilitates extraction of the key topological properties of the system. There are multiple ways to do this, some of which are more suitable for small systems and some for large aggregated datasets. These are outlined below, with examples given in figure 2.3, in reference to the small crystalline and amorphous configurations discussed in figure 2.2.

- **Persistence barcode**: represents the lifetime of each topological feature as a bar, starting at the birth value and terminating at the death value (see figures 2.3a, 2.3b). The barcode therefore contains all information about each feature, and whilst useful for small samples, it becomes difficult to interpret when there are a large number of features. In addition short lived features are difficult to identify.

- **Evolution in Betti numbers**: plots the total number of each n-dimensional feature for each filtration value (see figures 2.3c, 2.3d), and so provides more coarse-grained information than the barcode. It is equivalent to counting the number of bars at a specific filtration value.

- **Persistence diagram**: plots the birth and death value pairs, (b, d), of each feature as a scatter diagram (see figures 2.3e, 2.3f). This gives a more holistic view of the data as a whole. For large data sets, histogramming can be used, with points coloured by their relative multiplicities. The persistence diagram is therefore suitable for visualising large amounts of aggregate information.

For all these visualisation methods, it is worth emphasising that the filtration value, ϵ, has units of length, and so is normally quoted in terms of the equilibrium bond length, r_0.

Although these visualisation methods have been introduced here, they will be interpreted only at a very high level, with more detailed analysis provided in the analysis sections. Examining the results for the two example systems in 2.3, one can see that the crystalline and amorphous systems have both similarities and differences. To begin with, the 0-dimensional features appear very similar across all plots, with $b = 0$ and $d = r_0/2$. This is because in atomic systems, the average bond length is highly restricted, and so all atoms become connected in a very small range of filtration values, corresponding to half the mean bond length (as the filtration value measures the circumradius of the 1-simplex). As such, the 0-dimensional features provide little insight for atomic systems, and will be neglected in the analysis in this chapter.

On the other hand, the 1-dimensional features show significant differences between the crystalline and amorphous configurations. Both systems have 24 persistent bars in their barcode (figures 2.3a, 2.3b), which are born at $b = \epsilon = r_0/2$, but the lifetimes vary considerably. For the crystalline system, all persistent cycles (corresponding to hexagons) terminate at almost the same value of $\epsilon = r_0$, whereas in the amorphous case there is a much broader distribution of values. These values will be discussed in detail in section link , but as might be expected, it is related to the radius of the circumcircle into which each polygon is inscribed. It is not only the persistent cycles which show variation though. The persistence diagrams, figures 2.3e and 2.3f, also show that the short lived features, which lie close to the line $b = d$, show greater variation in the amorphous case. This will also be explored in greater depth in the remainder of the chapter.

What these small examples serve to demonstrate, is that persistent homology does show some promise for capturing the disorder in amorphous materials. The question is whether these visualisations can be systematically interpreted to quantify this disorder, and obtain information which is not available via alternative methods.

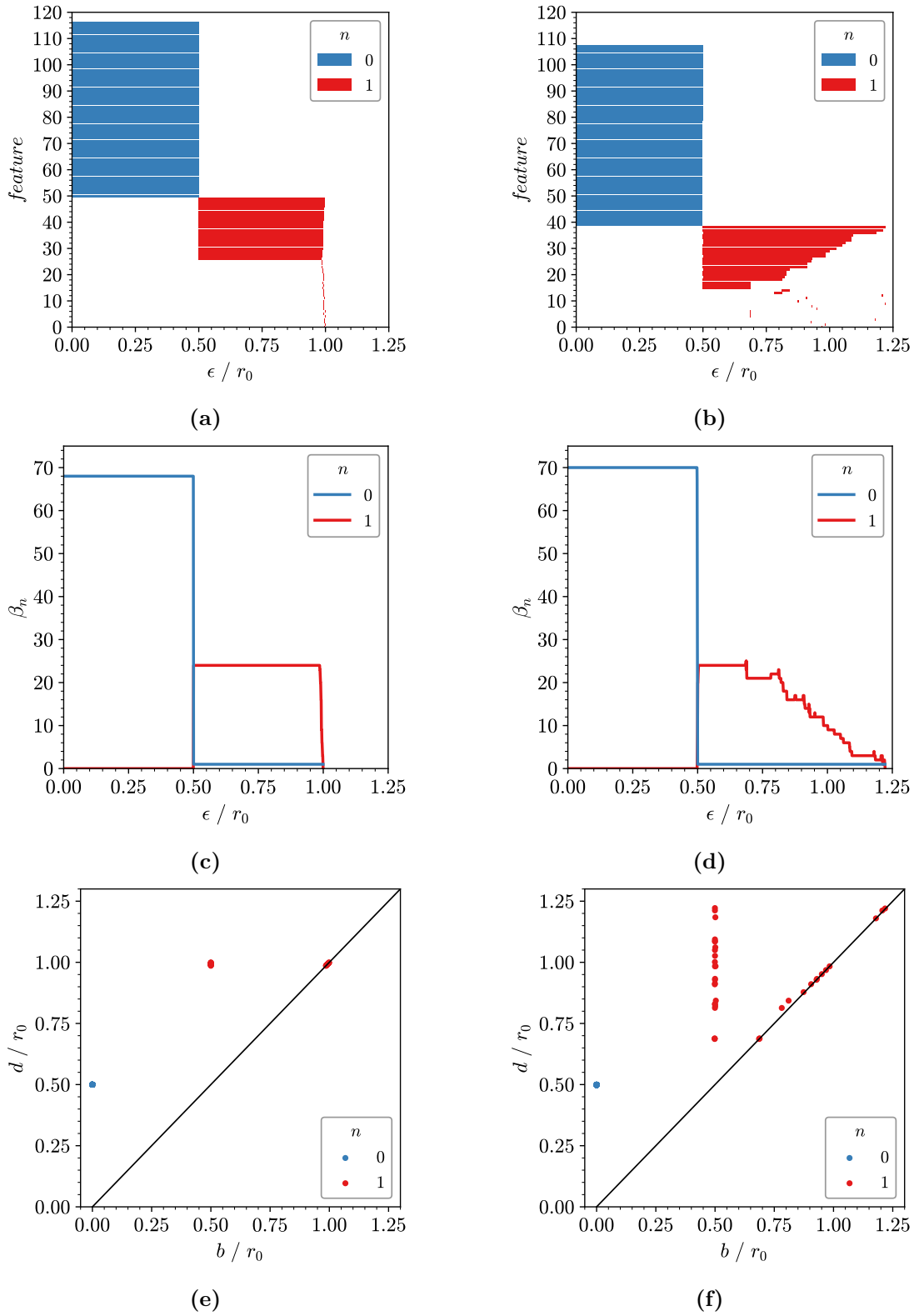

Figure 2.3: Different methods for visualising results of persistence of topological features. The left column gives results for the example crystalline configuration in figure 2.2, and the right column the amorphous configuration in the same figure. Panels (a), (b) show the persistence barcode, panels (c), (d) the evolution in Betti numbers with filtration value and (e), (f) the persistence diagram.

2.3 Persistent Homology with Triangle Rafts

Persistent homology is first studied in reference to triangle rafts, introduced in chapter link . To briefly reiterate, triangle rafts are a model for two-dimensional amorphous silica, representing the bilayer of corner sharing tetrahedra as projected equilateral triangles. Triangle rafts are characterised by having a diverse ring distributions, owing to the flexibility afforded to the structure by the oxygen linkages. Coupled with this, the Si-Si distances remain in a relatively tight distribution, as shown in table 2.1, as a result of the rigidity afforded by the triangular subunits.

Table 2.1: Relative Si-Si distances within different ring sizes in a triangle raft, assuming ring regularity.

k	4	5	6	7	8	9	10
Si-Si	0.966	0.995	1.000	0.997	0.991	0.985	0.978

An algorithm to construct triangle rafts was introduced in section link . The ring statistics in the resulting configurations can be tuned with a "temperature" parameter, T, with a higher temperature leading to the incorporation of more extreme ring sizes. This is beneficial, as it allows a systematic evaluation of the results of persistent homology calculations, using configurations with a continuous evolution in structure. As such, the samples from sections link , with ring sizes in the range $k = 4 \rightarrow 10$, were analysed using the GUDHI library [232]. In these analyses, only the silicon positions were included, as again the oxygen positions are in a sense "degenerate" (as they do not affect the ring topologies) and would only serve to obscure the calculation. In addition, this makes the cycles computed by persistent homology consistent with the definitions of rings elsewhere in this thesis.

The results of the persistent homology calculations will be discussed primarily in terms of the persistence diagrams, with the structure rationalised in comparison to analytic examples. However, it will also be shown how metrical quantities such as the ring statistics compare to persistent cycles.

2.3.1 Overview of Persistence Diagrams

The persistence diagrams for triangle rafts at four increasing temperatures are shown in figures 2.4a-2.4d, combined across multiple configurations. Discussing first the overall structure, one can see there is a definite systematic evolution in behaviour as temperature (and therefore disorder) increases. To aid discussion points will be referred to in terms of birth-death pairs, (b, d). At the lowest temperature, configurations are dominated largely by regular hexagons with few defects, reflected in the persistence diagram by bright spots at $(0.5, 1.0)$ and $(1.0, 1.0)$ (in comparison with figure 2.3e). As the temperature increases, and rings of different sizes are introduced, characteristic bands form in the persistence diagram, which are most intense at low lifetimes (*i.e.* close to $b = d$) and then "wash out" at lower birth values and longer lifetimes. At higher temperatures still, these bands broaden and finally coalesce.

This band structure and its associated behaviour has been observed before in studies of three-dimensional amorphous silica [**Robins2017**, 228, 230]. These papers often identify spots in the bands which correspond to known structures, and Hiraoka *et al.* go as far as suggesting that the bands correspond to rings formed from different nearest-neighbour length scales [228]. However, this was proposed by observing the cycles directly, and the interpretation is somewhat more complicated by the inclusion of oxygen atoms. By studying this problem in two dimensions, it can now be shown that these bands arise from the formation of rings between nearest-neighbour, second nearest-neighbour, and successively higher order interactions.

2.3.2 Band Structure in Persistence Diagrams

Before rationalising the band structure observed in the persistence diagrams of triangle rafts, it is useful to consider again the process of cycle formation in persistent homology. The important points are summarised below:

1. A cycle is born when a 1-simplex cuts a previous cycle in two. The birth value of the new cycle is then equal to the filtration value of the 1-simplex.

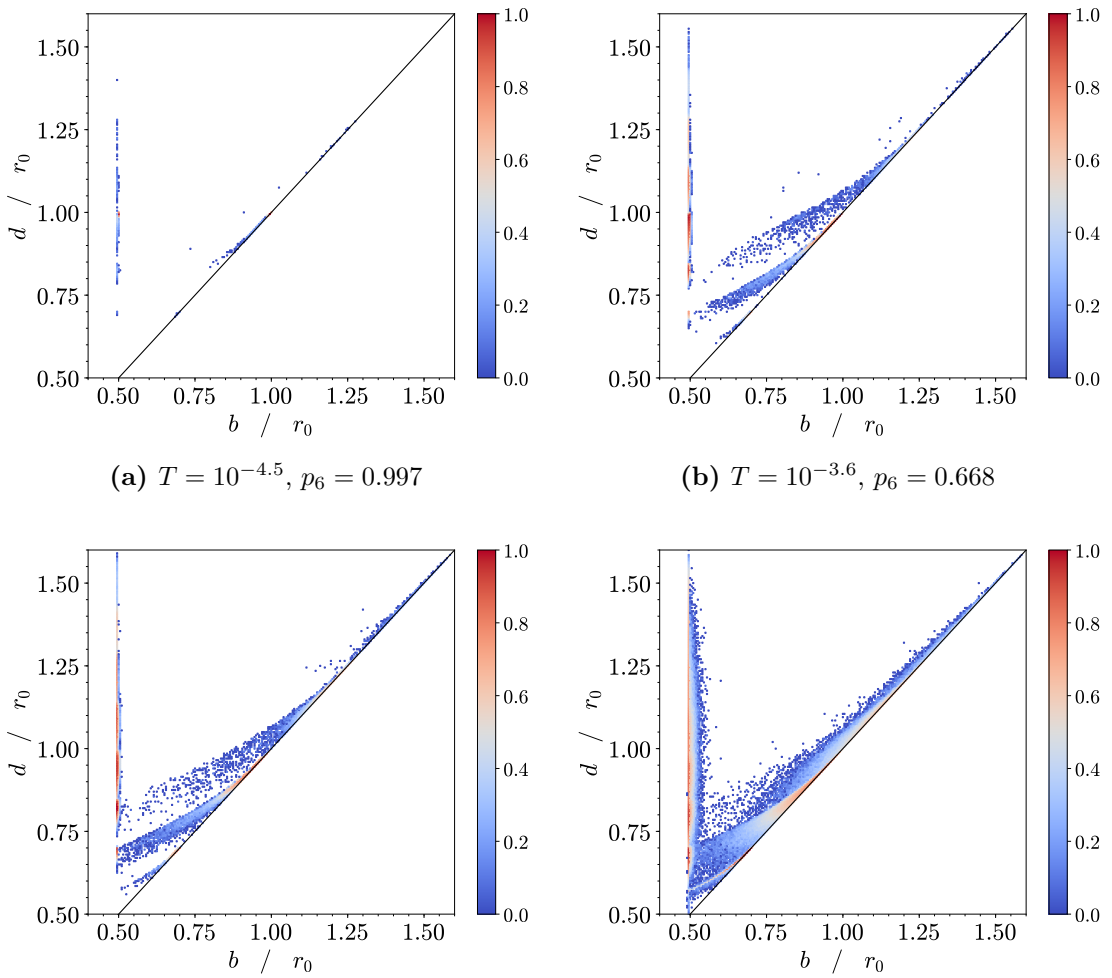

(a) $T = 10^{-4.5}$, $p_6 = 0.997$

(b) $T = 10^{-3.6}$, $p_6 = 0.668$

(c) $T = 10^{-2.7}$, $p_6 = 0.354$

(d) $T = 10^{-1.8}$, $p_6 = 0.211$

Figure 2.4: Persistence diagrams for triangle rafts generated at increasing temperatures and disorder (as indicated in captions). Points are coloured by multiplicity to highlight structure. The line $b = d$ is also indicated as a diagonal black line.

2. A cycle dies dies when *all* of the 2-simplices within it are present. The death value is then equal to the highest filtration value of the constituent 2-simplices.

3. A cycle is only counted if the death value is strictly greater than the birth value.

4. As a result of the above, a cycle will only persist if the 1-simplex which creates it has a lower filtration value than the 2-simplex which destroys it.

Understanding these properties is key to interpreting the results of persistence diagrams.

To explore the origins of the band structure, an ideal set of polygons will primarily be considered, where all sides have unit length. As previously mentioned, this approximation is reasonable for triangle rafts. The first, and simplest, band to consider is the vertical band at $b = 0.5$, which displays bright spots along its length. These correspond to the cycles initially formed when 1-simplices connect adjacent atoms, which have a circumradius of half the edge length. This band therefore originates from cycles pertaining to the nearest-neighbour interactions, and so will be referred to as the band B_1. These cycles will only die when all the 2-simplices inside them are present. As an illustration, a model is introduced whereby cycles are treated as a regular polygon with unit side lengths. By definition, in this case all simplices must have the same filtration value, as they lie on a common circle (see for example figure 2.5b). The filtration values for these simplices are given by:

$$\Phi_k = \frac{1}{2\sin(\pi/k)}\,, \tag{2.1}$$

where Φ_k will be used to denote the circumradius in a regular k-sided polygon with unit edge lengths. The values of Φ_k for $4 \leq k \leq 10$ can be found in table 2.2. It follows that a regular polygon will have a death value at Φ_k, and furthermore, no more cycles will be born out of this point set. Although difficult to see, these correspond well with the bright spots in the persistence diagrams in figure 2.4, as will be more apparent in subsequent analyses in this chapter.

Table 2.2: Circumradii of regular polygons with unit edge lengths.

k	4	5	6	7	8	9	10
Φ_k	0.707	0.851	1.000	1.152	1.307	1.462	1.618

However, the vertical band clearly shows a continuum of values, not discrete points. Therefore, a modification to the model can be considered, whereby all edge lengths are maintained at unity, but the polygon undergoes a systematic distortion - begin compressed about an axis passing through two opposite edges. This process is highlighted in figures 2.5a-2.5e. In this part of the analysis, only the persistence cycles which are born at $b = 0.5$ are of interest. These cycles will

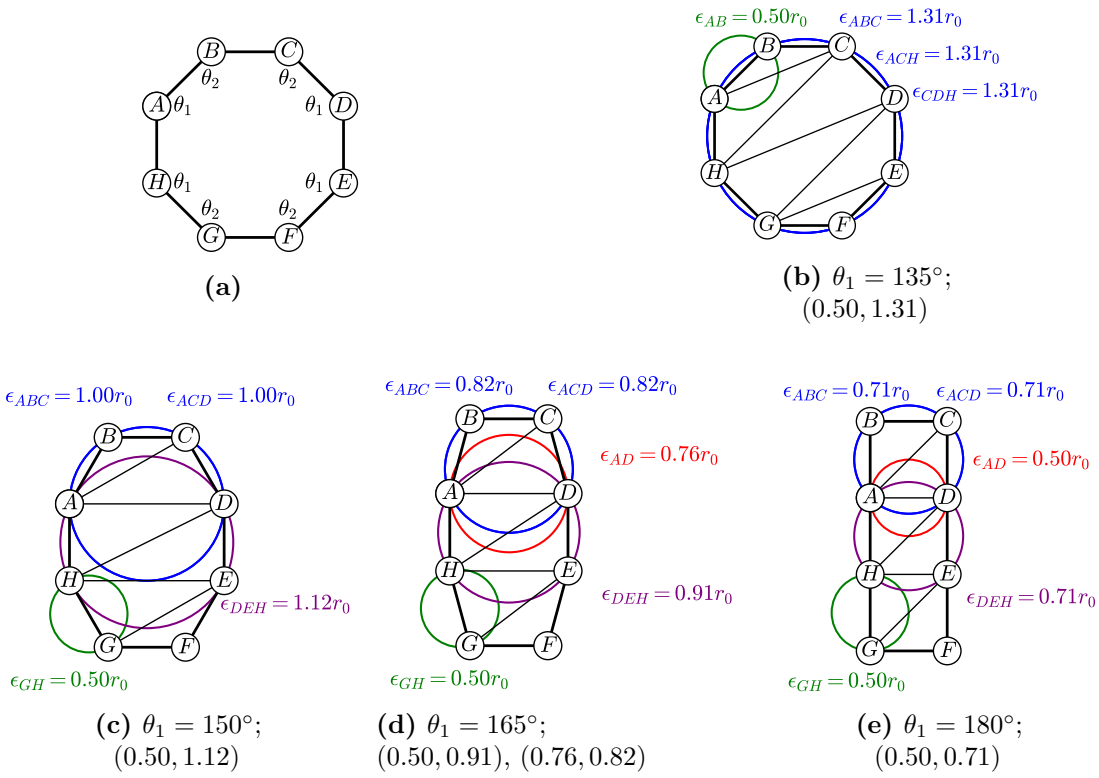

(a)

(b) $\theta_1 = 135°$; $(0.50, 1.31)$

(c) $\theta_1 = 150°$; $(0.50, 1.12)$

(d) $\theta_1 = 165°$; $(0.50, 0.91)$, $(0.76, 0.82)$

(e) $\theta_1 = 180°$; $(0.50, 0.71)$

Figure 2.5: Systematic distortions of an octagon with unit side lengths, and the effect on the corresponding persistent cycles. Panel (a) shows the octagon model, which is defined in terms of two angles. Panels (b)-(e) show a series of distortions. For each panel the angles and persistence (b, d) pairs are given in the caption. In addition, the circumcircles of selected simplices are highlighted, with the corresponding filtration values colour coded. The Delaunay triangulation is given as the interior black lines. These diagrams outline the origin of the B_1 and B_3 bands.

die when the Delaunay triangulation is realised. This is achieved when the simplex with the highest filtration value, here DEH or ADH, is present. As the polygon is compressed, it can be seen that the circumcircle for this simplex (purple circle) is reduced. In other words, distortion of the polygon acts to reduce the lifetime of the original cycle born at $b = 0.5$. The consequence of this is that the band B_1 manifests, instead of a simple series of discrete points.

The distortions in figures 2.5a-2.5e demonstrate the phenomenon central to the discussion of the remaining bands. As can be seen, between some critical values of θ, a second cycle is born within the first. This is only possible when the 1-simplex AD has a filtration value less than the 2-simplex ACD. In figure 2.5c where $\theta_1 = 150°$, this is *not* the case, as AD and ACD share the same filtration value. This is in

fact the limiting case, and beyond this angle the circumcircle for AD (red circle) is not contained within that for ACD (blue circle), and has a smaller radius, and therefore filtration value. The persistence of this cycle will therefore range between $(0.5, 0.71)$, $(0.76, 0.82)$ and $(1.0, 1.0)$. The intermediate values can be found via numerically scanning the angle range, but even from these points it is clear that this corresponds well with the most prominent "central" band in the persistence diagram. Furthermore, this band arises from the cycles formed by connecting neighbours three bonds apart. Although shown for the octagon here, this in fact holds for the other ring sizes that can support this (*i.e.* $k > 5$), and so this band is termed B_3.

It might now be clear that the other bands can also be related to specific nearest-neighbour interactions. In order to demonstrate this, again the octagonal case can be examined, but with different ring distortions. Now compression is about an axis through two opposite vertices, outlined in figure 2.6. Figures 2.6c-2.6e illustrate how secondary cycle can be born at relatively high filtration values. Here compression causes the 1-simplex AE to have a filtration value lower than the 2-simplex ADE, enabling formation of a second cycle. The atoms A, E are separated by four bonds and so the corresponding band for such species is B_4. The as-yet unaccounted for band, at the lowest persistence, naturally must be B_2, arising from atoms separated by two bonds. Examples of the formation of B_2 in the octagon are given in figures 2.6f-2.6h, corresponding to a "pinch".

As can be seen, for the octagon it is relatively difficult to add to the B_2 band. This is worth some consideration. It has been stated that this analysis is not unique to the octagon, which has merely been selected for illustrative purposes as it *can* display all the required behaviour. However, in general large polygons ($k > 6$) require little distortion to yield B_3 and B_4 bands, whereas significant rearrangement would be needed to contribute to B_2. On the other hand, the B_2 band readily forms for small polygons $k < 6$ and indeed the higher bands are inaccessible. The most common polygon, the hexagon, most easily forms secondary cycles in B_3, and to a lesser extend B_2. This explains the relative prominence of this central B_3 band in figures 2.4a-2.4d. Furthermore, it is equally possible to obtain higher bands still,

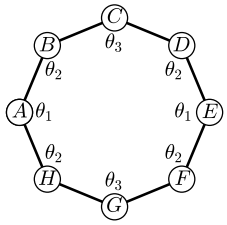

(a)

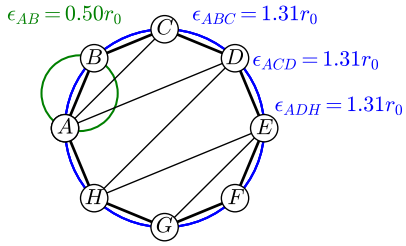

(b) $\theta_1 = 135°$, $\theta_2 = 135°$; $(0.50, 1.31)$

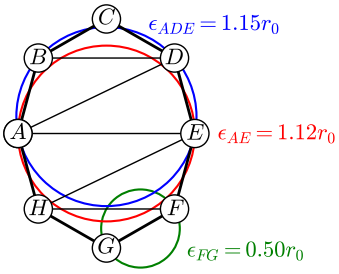

(c) $\theta_1 = 150°$, $\theta_2 = 135°$; $(0.50, 1.15)$, $(1.12, 1.15)$

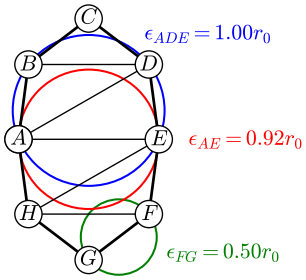

(d) $\theta_1 = 165°$, $\theta_2 = 135°$; $(0.50, 1.00)$, $(0.92, 1.00)$

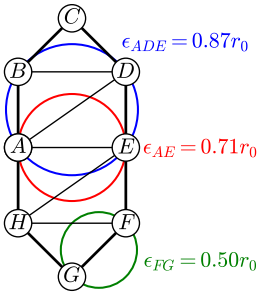

(e) $\theta_1 = 180°$, $\theta_2 = 135°$; $(0.50, 0.87)$, $(0.71, 0.87)$

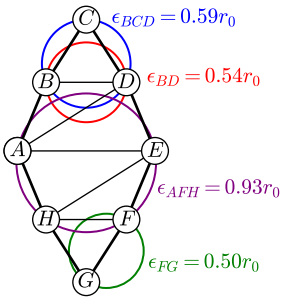

(f) $\theta_1 = 135°$, $\theta_2 = 170°$; $(0.50, 0.93)$, $(0.54, 0.59)$

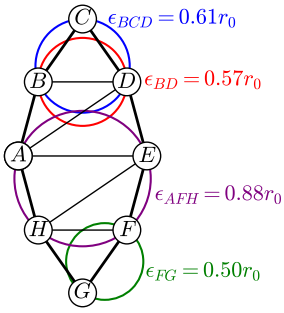

(g) $\theta_1 = 150°$, $\theta_2 = 160°$; $(0.50, 0.88)$, $(0.57, 0.61)$

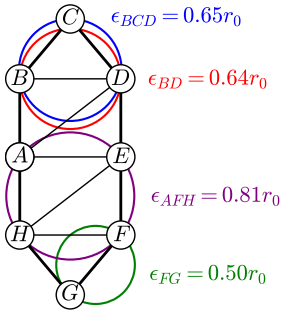

(h) $\theta_1 = 180°$, $\theta_2 = 140°$; $(0.50, 0.81)$, $(0.64, 0.65)$

Figure 2.6: Further systematic distortions of an octagon with unit side lengths, and the effect on the corresponding persistent cycles. Panel (a) shows the octagon model, which is defined in terms of three angles. Panels (b)-(h) show a series of distortions. For each panel the angles and persistence (b, d) pairs are given in the caption (for panels (f)-(h) an additional cycle is present, contributing to B_3, which is omitted for simplicity). In addition, the circumcircles of selected simplices are highlighted, with the corresponding filtration values colour coded. The Delaunay triangulation is given as the interior black lines. These diagrams outline the origin of the B_2 and B_4 bands.

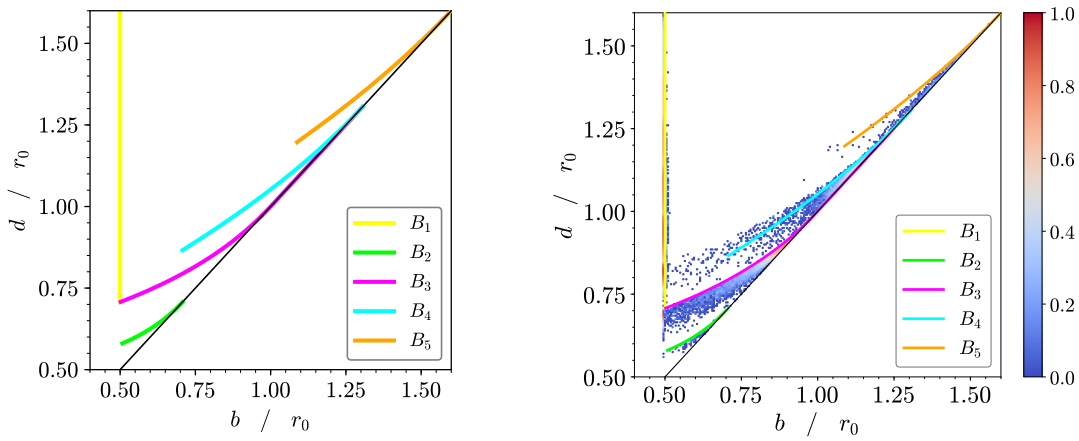

(a) **(b)**

Figure 2.7: Bands corresponding to different nearest-neighbour interactions, as calculated numerically using idealised models. Panel (a) shows the isolated lines, whilst panel (b) overlays them on the persistence diagram for triangle rafts from figure 2.4c, to which there is good agreement

.

with sufficiently large polygons. In the case of the triangle rafts in this section, the decagon in fact leads to the presence of a weak B_5 band.

To conclude this section, the reasoning outlined above is tested by generating the bands numerically (distorting polygons conforming to the various idealised models), and comparing to the persistence diagrams of triangle rafts. The results are given in figure 2.7, which are quite compelling. The shapes and positions of the various bands match well with those in the persistence diagrams from triangle rafts. Furthermore, the intensities agree with the previous discussion, with the B_3 band being by far the most prominent. It should be noted that the B_3 band calculated from the idealised model corresponds to the upper limit of that found from triangle raft simulations. This is also as expected, as distortions in bond lengths and will only serve to reduce the death value. This is because, as table 2.1 shows, the nature of the triangle raft model (of hinged near-rigid triangles), means that the bond lengths can only be less than the equilibrium value, which leads to a concomitant decrease in the circumradii. Overall, the relative simplicity and rigidity of the triangle raft model has enabled the structure of persistence diagrams to be well understood in this two-dimensional case.

2.3.3 Cycles, Betti Numbers and Ring Statistics

In addition to the persistence diagrams, information is also available through the first Betti number, β_1, which quantifies the number of cycles present at specific filtration value. Plotting the β_1 against ϵ therefore reveals how the number of cycles grows and decays across the range of filtration values [230]. As will be shown, this allows characterisation of the proportion of cycles with k vertices, termed here k-cycles. The advantage of using configurations from computation is, as ever, that the these cycles can be compared to known quantities which are known and directly calculated in the computational algorithm, in this case the ring statistics.

Plots of the evolution of the first Betti number with filtration are given in 2.8, for triangle rafts constructed at different temperatures. Each configuration contains 1000 rings, but the data are averaged over all 100 configurations produced at the same temperature. Note that there are two subtly different calculations presented here. The first, figure 2.8a, gives β_1 for all cycles found via persistent homology, whilst the second, figure 2.8b, gives β_1 only for the 1000 most persistent cycles (*i.e.* those with the longest lifetime). The rationale here is that the second case will only include cycles in the B_1 band, excluding those in the higher order bands, and hence should correspond most closely to the known ring structure. In fact, both sets of results are very similar (which will be discussed in due course), and so can be considered together.

As is now expected, β_1, rises very sharply from $0 \rightarrow 1000$ at $\epsilon = 0.5$, as the first cycles form at half the bond distance. The value of β_1 must then decay to zero in the limit of $\epsilon \rightarrow \infty$, but the form of the curve varies with the system temperature. At the lowest temperature, which is primarily a hexagonal lattice, the function is almost a step function at $\epsilon = 1.0$, but as the temperature increases, and more diverse ring sizes are incorporated, the curve broadens and smoothens. Even for the highest temperature, the decay in β_1 is not however smooth, but a series of stepwise decrements. These decrements align very closely to the values of the circumradii of k-polygons with unit edge lengths, Φ_k, given in table 2.2. As discussed in the previous section, Φ_k represents the upper bound on the death value

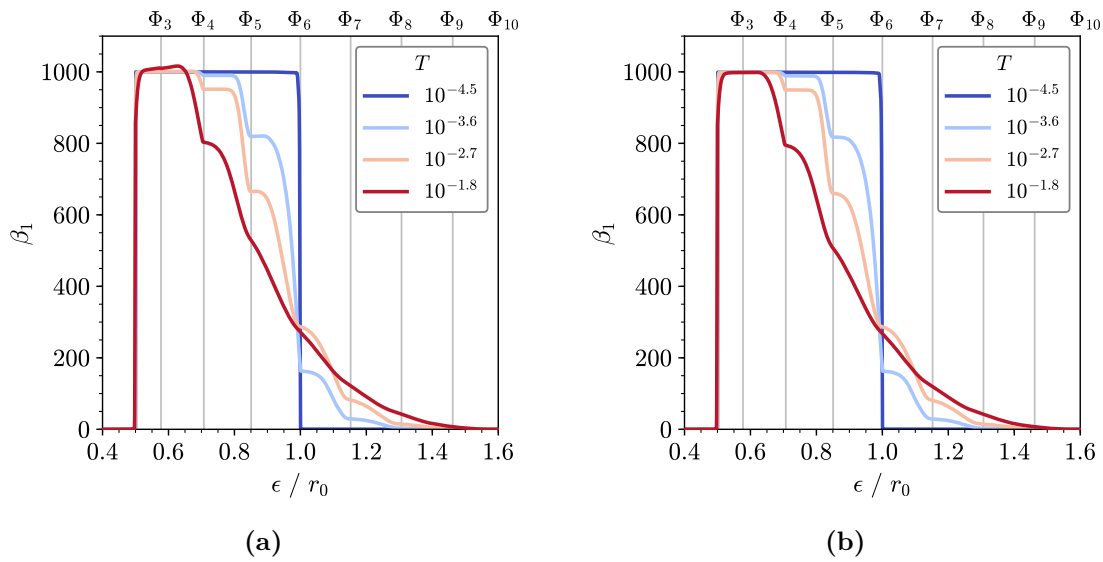

Figure 2.8: Evolution of the first Betti number with filtration for triangle rafts at different levels of disorder. In panel (a) the calculation includes all cycles, whereas panel (b) includes only the 1000 most persistent cycles. The circumradii of regular polygons with k vertices, Φ_k, are indicated by vertical grey lines.

for a k-polygon in B_1, for triangle rafts. Any deviations from regularity therefore act to reduce the lifetime. This largely explains the full behaviour of the curves in figure 2.8. The discontinuities represent changes between successive k-cycles dying, with the broadening of the curve indicative of the increasing variety of k values, and the smoothening the increased polygon distortion - both of which increase with temperature. It is interesting to note that the secondary cycles do not seem to affect the Betti numbers to a large degree, as evidenced by the similarity of figures 2.9a and 2.9b. Only at the highest temperature is there a detectable presence in the region between $\epsilon = 0.5 \rightarrow 0.7$. This is because these species are so relatively short-lived and spread throughout the filtration range, that at any filtration value they add a virtually insignificant contribution to the total.

With this logic, it should be possible to extract the cycle statistics, which will be denoted p_k, in analogy with ring statistics. To do so, one simply needs to calculate:

$$p_k = \beta_1 (\Phi_k) - \beta_1 (\Phi_{k-1}) \ , \tag{2.2}$$

and normalise across all k values. The cycle statistics from this process are given in figure 2.9a, which can be considered in reference to the ring statistics in figure

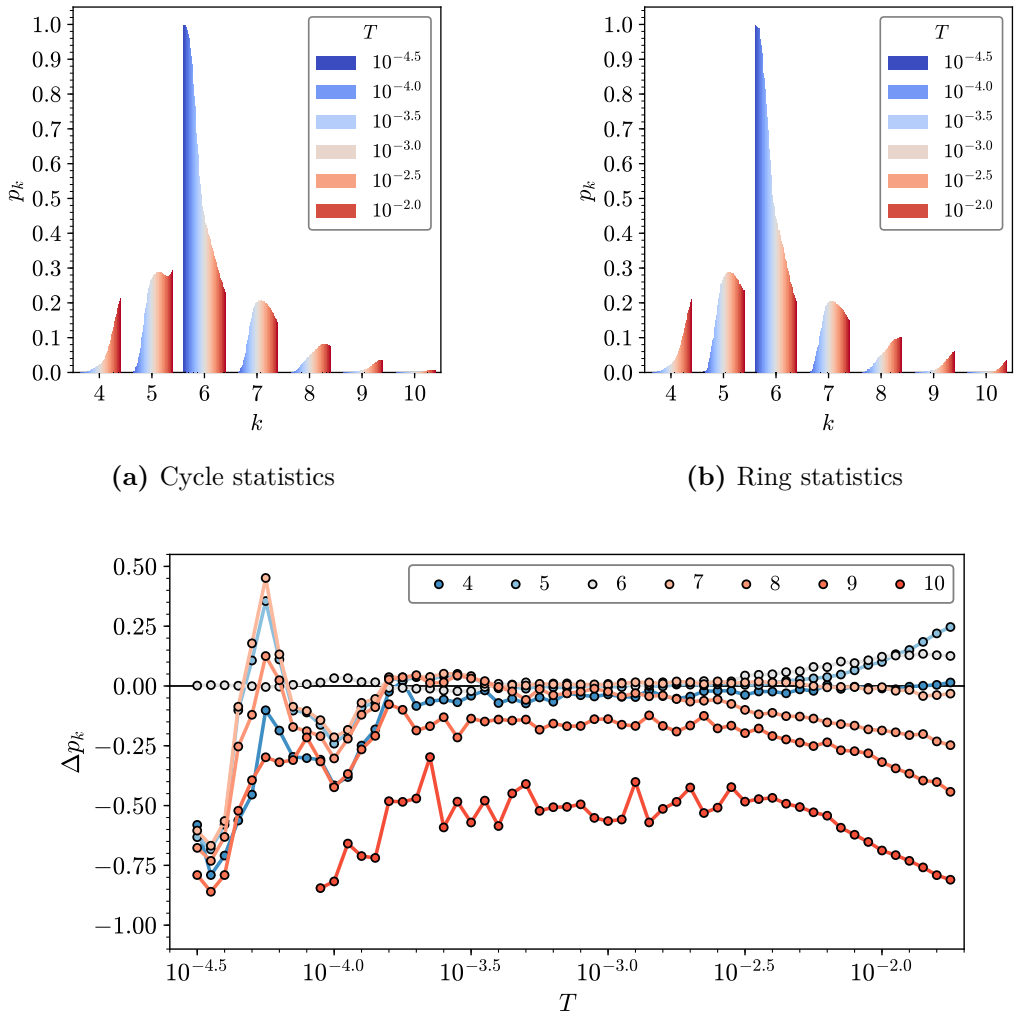

(a) Cycle statistics

(b) Ring statistics

(c)

Figure 2.9: Comparison of the k-cycle statistics, panel (a), against the ring statistics, panel (b), in triangle rafts across different levels of disorder. Panel (c) gives a direct comparison between the two.

2.9b. In addition, the comparative measure,

$$\Delta p_k = \frac{p_k^{\text{cycles}} - p_k^{\text{rings}}}{p_k^{rings}}, \tag{2.3}$$

is given in figure 2.9c. As can be seen, to a first approximation the agreement is very good, particularly for the ring sizes close to $k = 6$, at modest temperatures. This means that the cycles computed via persistent homology agree well with the primitive rings in the system, taking account for the approximative method to calculate k-cycles. Deviations are accentuated at very low temperature, when the absolute ring statistics of non-six rings are small, or at high temperatures, when

rings are increasingly distorted. For example, it is clear that p_{10} is systematically underestimated from cycles across the whole temperature range. In addition, the statistics of smaller rings ($k \leq 6$) are overestimated and larger rings ($k \geq 8$) underestimated increasingly at higher temperatures. The reason for this is that when large rings become sufficiently distorted, for instance becoming very elongated or even slightly non-convex, the cross ring distances become sufficiently small that they die much earlier than expected. Examining the polygons in figure 2.5a and 2.6a, and referring again to table 2.2, one can see that almost all of these examples would be classified as being of a smaller cycle size than they are in reality, when examining the death values. Considering all these factors, overall in two dimensions, for triangle rafts, it is reasonable to conclude that the cycles found from persistent homology are in almost exact accordance with the primitive rings in the system.

2.4 Persistent Homology with CRNs

The results of persistent homology with triangle rafts led to a well defined band structure in the persistence diagrams, as a consequence of the tightly controlled ring geometries. This structure is not always observed in simulations, for example with Cu-Zr alloys and high density molecular liquids [228, 229]. In these cases, more diffuse diagrams are found, which naturally accompanies the increase in degrees of freedom in such systems. The triangle raft algorithm is unable to directly reproduce these effects in two dimensions, owing to the innate rigidity of the model. However, this can be achieved with another algorithm developed in this thesis, namely bond switching link . In bond switching, the potential model allows for greater freedom in the bond lengths and angles, and the process of randomising an existing lattice (as opposed to building an random ring structure sequentially) allows configurations with a greater range of ring sizes, and a greater level of ring disorder, to be realised.

Therefore, in this section, persistent homology analysis will be performed on the configurations generated from bond switching, applying the information learned from analogous calculations on triangle rafts. The specific systems studied will be a subset of those from chapter link , namely those at two different bond stretching

and angle force constant ratios of $k_r/t_\theta = 16, 4$, with convexity maintained. The persistence diagrams and change in Betti numbers will be investigated for these systems, and the effect of the potential model highlighted. In addition, the results will be contrasted with those of triangle rafts.

2.4.1 Persistence Diagrams

The persistence diagrams for bond switching configurations generated with the two potential models are given in figure 2.10. Figures 2.10a-2.10d pertain to the force constant ratio $k_r/k_\theta = 16$ and figures 2.10e-2.10h at $k_r/k_\theta = 4$. For both models, four different p_6 values were selected, corresponding to four increasing levels of disorder. The initial impression may be that the persistence diagrams look very different from those of triangle rafts in figure 2.4, but closer inspection reveals this is not the case, and they share many of the same characteristics. A key point these apparent differences is that the bond lengths have inherently more flexibility in the case of bond switching than triangle rafts. As such, any similar features will appear much broader, but retain similar structural origins. For example, the B_1 band is present in all the diagrams in figure 2.10, centred around $b = 0.5$. The difference is that at low levels of disorder (see for example figures 2.10a-2.10b), one can clearly see distinct "spots" in B_1, which are present in figures 2.4 but harder to detect due to the narrowness of the band. The upper limits of these spots correspond well with the circumradii in table 2.2 *i.e.* they are related to the occurrence of specific k-cycles. At higher disorder these spots begins to coalesce, as in figure 2.10c, before fully combining to form a single high density feature, as in figure 2.10d. This final diagram can be considered "typical" of a highly disordered amorphous or liquid state [228, 229]. By using the bond switching method, it is clear however that this originates from the broadening and aggregation of features relating to individual cycle sizes. Other bands in the persistence diagram are also detectable, in particular B_3, but largely only at higher p_6 values. This is because these bands only occur when there are well defined large cycles. In bond switching, although there are primitive rings which are very large, these can become so distorted that they are

not calculated as a single persistent cycle, but rather multiple smaller cycles. This precludes the formation of significant higher order bands as seen in triangle rafts.

As for the comparison between the different potential models, the effect of changing the force constant ratio appears relatively small. By comparing the persistence diagram of similar p_6 values, one can see there is a general broadening of the regions corresponding to each cycle size on reducing the bond stretch to angle ratio. The rationale for this trend is the same as for increasing temperature - that increasing the variation in nearest-neighbour interatomic distances comes with associated variation in the values at which cycles are born and die. The difference between potential models naturally becomes less pronounced as disorder increases, and the Monte Carlo temperature is effectively infinite, such that the final diagrams, figures 2.10d and 2.10h, are almost identical. In these diagrams, the B_1 line appears to become progressively angled, driven by the decreasing birth value of smaller cycles. This is likely because the birth filtration value of a cycle depends on the final 1-simplex to form. As a cycles becomes larger, the probability that all constituent 1-simplices will have filtrations less that $b = 0.5$ becomes increasingly unlikely compared to smaller cycles. The result of this is that smaller cycles, with lower death values, can also have progressively lower birth values, leading to the perceived tilting of the B_1 band.

2.4.2 Evolution in Betti Numbers

2.5 Chapter Summary

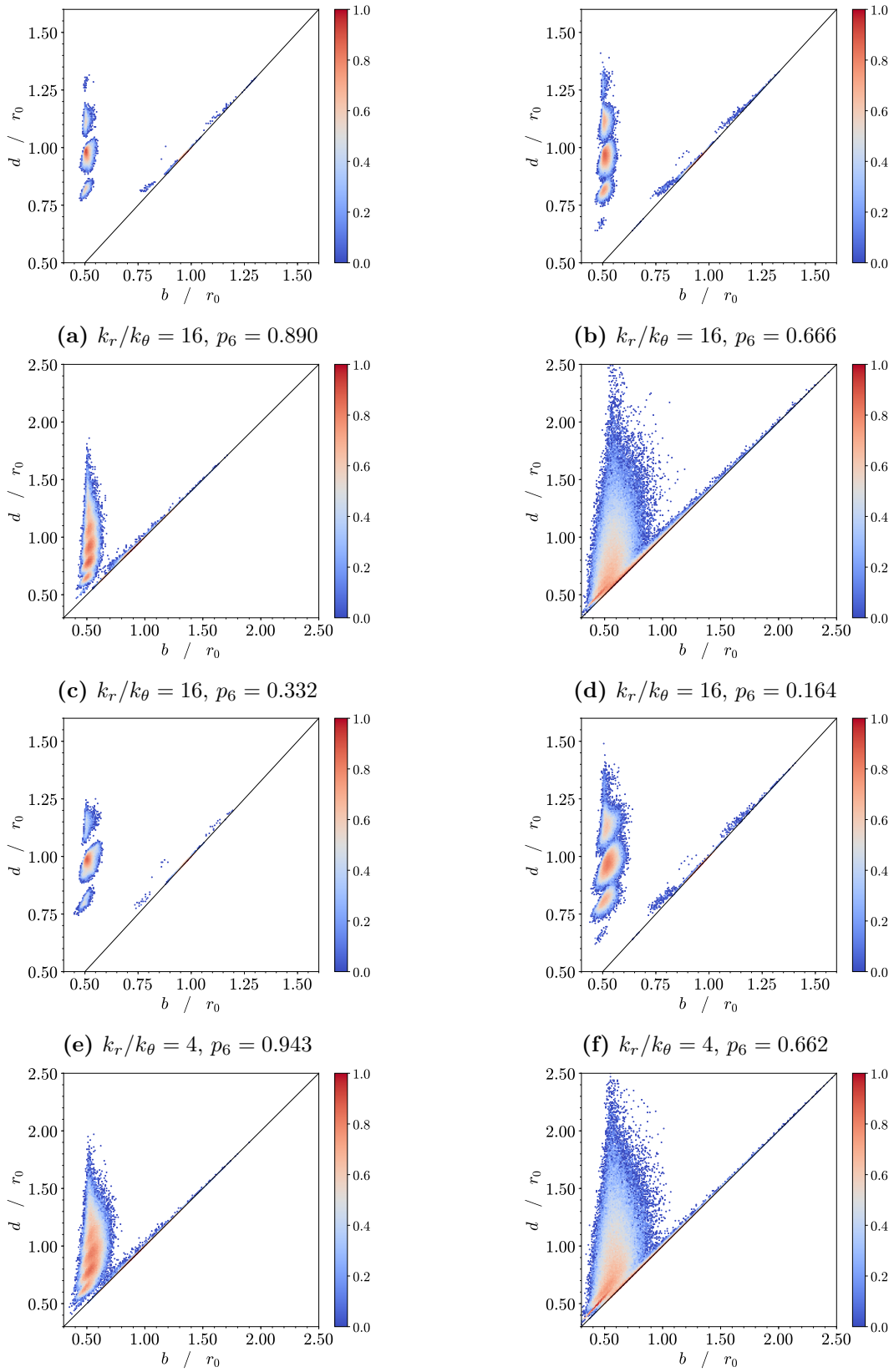

(a) $k_r/k_\theta = 16$, $p_6 = 0.890$

(b) $k_r/k_\theta = 16$, $p_6 = 0.666$

(c) $k_r/k_\theta = 16$, $p_6 = 0.332$

(d) $k_r/k_\theta = 16$, $p_6 = 0.164$

(e) $k_r/k_\theta = 4$, $p_6 = 0.943$

(f) $k_r/k_\theta = 4$, $p_6 = 0.662$

(g) $k_r/k_\theta = 4$, $p_6 = 0.332$

(h) $k_r/k_\theta = 4$, $p_6 = 0.163$

Figure 2.10: Persistence diagrams for configurations from bond switching, at different bond stretch/angle constants and p_6 (as indicated in captions).

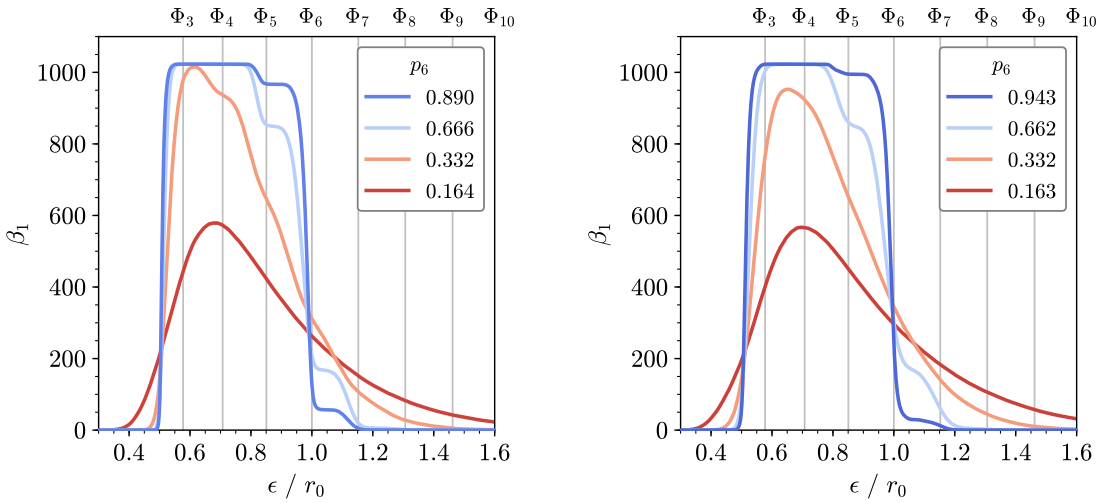

(a) $k_r/k_\theta = 16$ **(b)** $k_r/k_\theta = 4$

Figure 2.11: Evolution of the first Betti number with filtration for bond switching configurations at different levels of disorder and two different potential models (as indicated in captions).

Appendices

References

[1] W H Zachariasen. "The Atomic Arrangement in Glass". In: *J. Am. Chem. Soc.* 54.10 (1932), pp. 3841–3851.

[2] J. Kotakoski et al. "From point defects in graphene to two-dimensional amorphous carbon". In: *Phys. Rev. Lett.* 106 (2011), p. 105505.

[3] Alex W. Robertson et al. "Spatial control of defect creation in graphene at the nanoscale". In: *Nat. Commun.* 3 (2012), p. 1144.

[4] Pinshane Y Huang et al. "Direct Imaging of the a Two-Dimensional Silica Glass on Graphene". In: *Nano Lett.* 12 (2012), pp. 1081–1086.

[5] Leonid Lichtenstein, Markus Heyde, and Hans Joachim Freund. "Atomic arrangement in two-dimensional silica: From crystalline to vitreous structures". In: *J. Phys. Chem. C* 116 (2012), pp. 20426–20432.

[6] Shamil Shaikhutdinov and Hans-joachim Freund. "Metal-Supported Aluminosilicate Ultrathin Films as a Versatile Tool for Studying the Surface Chemistry of Zeolites". In: *ChemPhysChem* 14 (2013), pp. 71–77.

[7] Adrián Leandro Lewandowski et al. "Atomic structure of a metal-supported two-dimensional germania film". In: *Phys. Rev. B* 97 (2018), p. 115406.

[8] L Lewandowski et al. "From Crystalline to Amorphous Germania Bilayer Films at the Atomic Scale: Preparation and Characterization". In: *Angew. Chem. Int. Ed.* 58 (2019), pp. 10903–10908.

[9] Panagiotis Trogadas, Thomas F Fuller, and Peter Strasser. "Carbon as catalyst and support for electrochemical energy conversion". In: *Carbon N. Y.* 75 (2014), pp. 5–42.

[10] Yongfu Sun et al. "Ultrathin Two-Dimensional Inorganic Materials : New Opportunities for Solid State Nanochemistry". In: *Acc. Chem. Res.* 48 (2015), pp. 3–12.

[11] Christin Büchner and Markus Heyde. "Two-dimensional silica opens new perspectives". In: *Prog. Surf. Sci.* 92 (2017), pp. 341–374.

[12] Paul A Beck. "Annealing of cold worked metals". In: *Adv. Phys.* 3.11 (1954), pp. 245–324.

[13] C G Dunn and E F Koch. "Comparison of Dislocation Densities of Primary and Secondary Recrystallization Grains of Si-Fe". In: *Acta Metall.* 5 (1957), p. 548.

[14] A J Stone and D J Wales. "Theoretical Studies of Icosahedra C60 and Some Related Species". In: *Chem. Phys. Lett.* 128.5,6 (1986), pp. 501–503.

[15] J. Shackelford and B. D. Brown. “The Lognormal Distribution in the Random Network Structure”. In: *J. Non. Cryst. Solids* 44 (1981), pp. 379–382.

[16] J Lemaitre et al. “Arrangement of cells in Voronoi tesselations of monosize packing of discs”. In: *Philos. Mag. B* 67.3 (1993), pp. 347–362.

[17] Leonid Lichtenstein et al. “The atomic structure of a metal-supported vitreous thin silica film”. In: *Angew. Chemie - Int. Ed.* 51 (2012), pp. 404–407.

[18] D A Aboav. “Arrangement of grains in a polycrystal”. In: *Metallography* 3 (1970), pp. 383–390.

[19] D. Weaire. “Some remarks on the arrangement of grains in a polycrystal”. In: *Metallography* 7 (1974), pp. 157–160.

[20] Torbjörn Björkman et al. “Defects in bilayer silica and graphene: Common trends in diverse hexagonal two-dimensional systems”. In: *Sci. Rep.* 3 (2013), p. 3482.

[21] Andrei Malashevich, Sohrab Ismail-Beigi, and Eric I. Altman. “Directing the structure of two-dimensional silica and silicates”. In: *J. Phys. Chem. C* 120 (2016), pp. 26770–26781.

[22] Mark Wilson et al. “Modeling vitreous silica bilayers”. In: *Phys. Rev. B* 87 (2013), p. 214108.

[23] Mark Wilson and Harry Jenkins. “Crystalline thin films of silica : modelling , structure and energetics”. In: *J. Phys. Condens. Matter* 30 (2018), p. 475401.

[24] Jin Zhang. “Phase-dependent mechanical properties of two-dimensional silica films: A molecular dynamics study”. In: *Comput. Mater. Sci.* 142 (2018), pp. 7–13.

[25] Franz Bamer, Firaz Ebrahem, and Bernd Markert. “Athermal mechanical analysis of Stone-Wales defects in two-dimensional silica”. In: *Comput. Mater. Sci.* 163 (2019), pp. 301–307.

[26] Projesh Kumar Roy and Andreas Heuer. “Ring Statistics in 2D Silica: Effective Temperatures in Equilibrium”. In: *Phys. Rev. Lett.* 122 (2019), p. 016104.

[27] Nina F. Richter et al. “Characterization of Phonon Vibrations of Silica Bilayer Films”. In: *J. Phys. Chem. C* 123 (2019), pp. 7110–7117.

[28] Projesh Kumar Roy, Markus Heyde, and Andreas Heuer. “Modelling the atomic arrangement of amorphous 2D silica: a network analysis”. In: *Phys. Chem. Chem. Phys.* 20 (2018), pp. 14725–14739.

[29] Avishek Kumar et al. “Ring statistics of silica bilayers”. In: *J. Phys. Condens. Matter* 26 (2014), p. 395401.

[30] D. A. Aboav. “The arrangement of cells in a net. I”. In: *Metallography* 13 (1980), pp. 43–58.

[31] B. N. Boots. “Comments on "Aboav’s Rule" for the Arrangement of Cells in a Network”. In: *Metallography* 17 (1984), pp. 411–418.

[32] J. C. Earnshaw and D. J. Robinson. “Topological correlations in colloidal aggregation”. In: *Phys. Rev. Lett.* 72.23 (1994), p. 3682.

[33] C Allain and L Limat. “Regular Patterns of Cracks Formed by Directional Drying of a Collodial Suspension”. In: *Phys. Rev. Lett.* 74.15 (1995), p. 2981.

[34] A Moncho-Jorda, F Martinez-Lopez, and R Hidalgo-Alvarez. "Simulations of aggregation in 2D . A study of kinetics , structure and topological properties". In: *Physica A* 282 (2000), pp. 50–64.

[35] Marc Durand et al. "Statistical mechanics of two-dimensional shuffled foams: Prediction of the correlation between geometry and topology". In: *Phys. Rev. Lett.* 107 (2011), p. 168304.

[36] Mingming Tong et al. "Geometry and Topology of Two-Dimensional Dry Foams : Computer Simulation and Experimental Characterization". In: *Langmuir* 33 (2017), pp. 3839–3846.

[37] Lucas Goehring and Stephen W Morris. "Cracking mud, freezing dirt, and breaking rocks". In: *Phys. Today* 67.11 (2014), p. 39.

[38] D Brutin et al. "Pattern formation in drying drops of blood". In: *J. Fluid Mech.* 667 (2011), pp. 85–95.

[39] Franziska Glassmeier and Graham Feingold. "Network approach to patterns in stratocumulus clouds". In: *PNAS* 114.40 (2017), pp. 10578–10583.

[40] Michel C Milinkovitch et al. "Crocodile Head Scales Are Not Developmental Units But Emerge From Physical Cracking". In: *Science (80-.).* 339 (2019), pp. 78–81.

[41] G. Le Caër and R. Delannay. "The administrative divisions of mainland France as 2D random cellular structures". In: *J. Phys. Fr.* 3 (1993), p. 1777.

[42] G Schliecker and S Klapp. "Why are the equilibrium properties of two-dimensional random cellular structures so similar?" In: *Europhys. Lett.* 48.2 (1999), pp. 122–128.

[43] William T. Gibson et al. "Control of the mitotic cleavage plane by local epithelial topology". In: *Cell* 144 (2011), pp. 427–438.

[44] M Kokalj Ladan, P Ziherl, and A Šiber. "Topology of dividing planar tilings : Mitosis and order in epithelial tissues". In: *Phys. Rev. E* 100 (2019), p. 012410.

[45] D. Weaire and N. Rivier. "Soap, cells and statistics-random patterns in two dimensions". In: *Contemp. Phys.* 50.1 (2009), pp. 199–239.

[46] J C Flores. "Mean-field crack networks on desiccated films and their applications : Girl with a Pearl Earring". In: *Soft Matter* 13 (2017), pp. 1352–1356.

[47] Steven H Strogatz. "Exploring complex networks". In: *Nature* 410 (2001), p. 268.

[48] S Boccaletti et al. "Complex networks : Structure and dynamics". In: *Phys. Rep.* 424 (2006), pp. 175–308.

[49] Albert-László Barabási. "The network takeover". In: *Nat. Phys.* 8 (2012), pp. 14–16.

[50] Alice L. Thorneywork et al. "Two-Dimensional Melting of Colloidal Hard Spheres". In: *Phys. Rev. Lett.* 118 (2017), p. 158001.

[51] Andrew B Cairns et al. "Design of crystal-like aperiodic solids with selective disorder–phonon coupling". In: *Nat. Commun.* 7 (2016), p. 10445.

[52] Albert-László Barabási and Márton Pósfai. *Network science*. Cambridge: Cambridge University Press, 2016.

[53] Xianglong Yuan and A N Cormack. "Efficient algorithm for primitive ring statistics in topological networks". In: *Comput. Mater. Sci.* 24 (2002), pp. 343–360.

[54] D. A. Aboav. "The Arrangement of Cells in a Net. III". In: *Metallography* 17 (1984), pp. 383–396.

[55] E Ressouche et al. "Magnetic Frustration in an Iron-Based Cairo Pentagonal Lattice". In: *Phys. Rev. Lett.* 103 (2009), p. 267204.

[56] P W Fowler et al. "Energetics of Fullerenes with Four-Membered Rings". In: *J Phys Chem* 100 (1996), pp. 6984–6991.

[57] A. Gervois, J. P. Troadec, and J. Lemaitre. "Universal properties of Voronoi tessellations of hard discs". In: *J. Phys. A* 25 (1992), pp. 6169–6177.

[58] G. Le Caër and R. Delannay. "Correlations in Topological Models of 2d Random Cellular Structures". In: *J. Phys. A* 26 (1993), pp. 3931–3954.

[59] P Cerisier, S Rahal, and N Rivier. "Topological correlations in Benard-Marangoni convective structures". In: *Phys. Rev. E* 54.5 (1996), pp. 5086–5094.

[60] Matthew P. Miklius and Sascha Hilgenfeldt. "Analytical results for size-topology correlations in 2D disk and cellular packings". In: *Phys. Rev. Lett.* 108 (2012), p. 015502.

[61] N Rivier, D Weaire, and R Romer. "Tetrahedrally Bonded Random Networks Without Odd Rings". In: *J. Non. Cryst. Solids* 105 (1988), pp. 287–291.

[62] F. T. Lewis. "The correlation between cell division and the shapes and sizes of prismatic cell in the epidermis of cucumis". In: *Anat. Rec.* 38.3 (1928), pp. 341–376.

[63] M. A. Fortes. "Applicability of the Lewis and Aboav-Weaire laws to 2D and 3D cellular structures based on Poisson partitions". In: *J. Phys. A* 28 (1995), pp. 1055–1068.

[64] Sangwoo Kim, Muyun Cai, and Sascha Hilgenfeldt. "Lewis' law revisited: the role of anisotropy in size-topology correlations". In: *New J. Phys.* 16 (2014), p. 015024.

[65] S. N. Chiu. "Aboav-Weaire's and Lewis' laws - A review". In: *Mater. Charact.* 34 (1995), pp. 149–165.

[66] Renaud Delannay and Gérard Le Caër. "Topological characteristics of 2D cellular structures generated by fragmentation". In: *Phys. Rev. Lett.* 73.11 (1994), pp. 1553–1556.

[67] S Le Roux and F Rezai-Aria. "Topological and metric properties of microscopic crack patterns : application to thermal fatigue of high temperature". In: *J. Phys. D* 46 (2013), p. 295301.

[68] David A Noever. "Statistics of emulsion lattices". In: *Colloids and Surfaces* 62 (1992), pp. 243–247.

[69] J. C. M. Mombach, R. M. C. de Almeida, and J. R. Iglesias. "Two-cell correlations in biological tissues". In: *Phys. Rev. E* 47.5 (1993), pp. 3712–3717.

[70] P Pedro et al. "Polygonal terrains on Mars : A contribution to their geometric and topological characterization". In: *Planet. Space Sci.* 56 (2008), pp. 1919–1924.

[71] David P Landau and Kurt Binder. *A Guide to Monte Carlo Simulations in Statistical Physics*. 4th ed. Cambridge University Press, 2014.

[72] David J Wales and Harold A Scheraga. "Global Optimization of Clusters, Crystals, and Biomolecules". In: *Science (80-.).* 285 (1999), pp. 1368–1372.

[73] Andrea C Levi and Miroslav Kotrla. "Theory and simulation of crystal growth". In: *J. Phys. Condens. Matter* 9 (1997), p. 299.

[74] C Ratsch and J A Venables. "Nucleation Theory and the Early Stages of Thin Film Growth". In: *J. Vac. Sci. Technol. A* 21 (2003), S96.

[75] Wlater Kob. "Computer simulations of supercooled liquids and glasses". In: *J. Phys. Condens. Matter* 11 (1999), R85.

[76] Pablo Jensen. "Growth of nanostructures by cluster deposition: Experiments and simple models". In: *Rev. Mod. Phys.* 71.5 (1999), pp. 1695–1735.

[77] Daan Frenkel and Berend Smit. *Understanding Molecular Simulation: from Algorithms to Applications*. 2nd ed. Academic Press, 2002.

[78] M P Allen and D J Tildesley. *Computer simulation of liquids*. 2nd ed. Oxford Science Publications, 2017.

[79] Steve Brooks et al. *Handbook of Markov Chain Monte Carlo*. CRC Press, 2011.

[80] N Metropolis et al. "Equation of State Calculations by Fast Computing Machines". In: *J. Chem. Phys.* 21.6 (1953), pp. 1087–1092.

[81] Vasilios I Manousiouthakis and Michael W Deem. "Strict detailed balance is unnecessary in Monte Carlo simulation". In: *J. Chem. Phys.* 110 (1999), p. 2753.

[82] Hidemaro Suwa and Synge Todo. "Markov Chain Monte Carlo Method without Detailed Balance". In: *Phys. Rev. Lett.* 105 (2010), p. 120603.

[83] Manon Michel, Sebastian C Kapfer, and Werner Krauth. "Generalized event-chain Monte Carlo:" in: *J. Chem. Phys.* 140 (2014), p. 054116.

[84] G M Torrie and J P Valleau. "Nonphysical Sampling Distributions in Monte Carlo Free-Energy Estimation: Umbrella Sampling". In: *J. Comput. Phys.* 23 (1977), pp. 187–199.

[85] David J Earl and Michael W Deem. "Parallel tempering: Theory, applications, and new perspectives". In: *Phys. Chem. Chem. Phys.* 7 (2005), pp. 3910–3916.

[86] Bernd Hartke. "Global Geometry Optimization of Clusters Using Genetic Algorithms". In: *J. Phys. Chem.* 97 (1993), pp. 9973–9976.

[87] J A Niesse and Howard R Mayne. "Global geometry optimization of atomic clusters using a modified genetic algorithm in space-fixed coordinates". In: *J. Chem. Phys.* 105 (1996), p. 4700.

[88] David J Wales and Jonathan P K Doye. "Global Optimization by Basin-Hopping and the Lowest Energy Structures of Lennard-Jones Clusters Containing up to 110 Atoms". In: *J. Phys. Chem. A* 101 (1997), pp. 5111–5116.

[89] S . Kirkpatrick, C . D . Gelatt Jr., and M . P . Vecchi. "Optimization by Simulated Annealing". In: *Science (80-.).* 220.4598 (1983), pp. 671–680.

[90] Darrall Henderson, Sheldon H Jacobson, and Alan W Johnson. "The Theory and Practice of Simulated Annealing". In: *Handb. Metaheuristics*. Ed. by Fred Glover and Gary A Kochenberger. Boston, MA: Springer US, 2003, pp. 287–319.

[91] F Wooten, K Winer, and D Weaire. "Computer Generation of Structural Models of Amorphous Si and Ge". In: *Phys. Rev. Lett.* 54.13 (1985), pp. 1392–1395.

[92] M M J Treacy and K B Borisenko. "The Local Structure of Amorphous Silicon". In: *Science (80-.).* 335 (2012), pp. 950–953.

[93] Yuhai Tu et al. "Properties of a Continuous-Random-Network Model for Amorphous Systems". In: *Phys. Rev. Lett.* 81.22 (1998), pp. 4899–4902.

[94] B R Djordjevic, M F Thorpe, and F Wooten. "Computer model of tetrahedral amorphous diamond". In: *Phys. Rev. B* 52.8 (1995), pp. 5685–5690.

[95] Normand Mousseau and G T Barkema. "Binary continuous random networks". In: *J. Phys. Condens. Matter* 16 (2004), S5183–S5190. arXiv: `0408705 [cond-mat]`.

[96] E M Huisman, C Storm, and G T Barkema. "Monte Carlo study of multiply crosslinked semiflexible polymer networks". In: *Phys. Rev. E* 78 (2008), p. 051801.

[97] C P Broedersz and F C Mackintosh. "Modeling semiflexible polymer networks". In: *Rev. Mod. Phys.* 86 (2014), pp. 995–1036.

[98] Sandeep K Jain and Gerard T Barkema. "Rupture of amorphous graphene via void formation". In: *PCCP* 20 (2018), pp. 16966–16972.

[99] Avishek Kumar, Mark Wilson, and M F Thorpe. "Amorphous graphene: a realization of Zachariasen's glass". In: *J. Phys. Condens. Matter* 24 (2012), p. 485003.

[100] P. N. Keating. "Effect of invariance requirements on the elastic strain energy of crystals with application to the diamond structure". In: *Phys. Rev.* 145.2 (1966), pp. 637–645.

[101] G. Barkema and Normand Mousseau. "High-quality continuous random networks". In: *Phys. Rev. B* 62.8 (2000), pp. 4985–4990.

[102] D A Drabold. "Topics in the theory of amorphous materials". In: *Eur Phys J B* 68 (2009), pp. 1–21.

[103] S. von Alfthan, A. Kuronen, and K. Kaski. "Realistic models of amorphous silica: A comparative study of different potentials". In: *Phys. Rev. B* 68 (2003), p. 073203.

[104] Monica Bulacu et al. "Improved Angle Potentials for Coarse-Grained Molecular Dynamics Simulations". In: *J. Chem. Theory Comput.* 9 (2013), pp. 3282–3292.

[105] Jorge Nocedal and Stephen J Wright. *Numerical Optimization*. 2nd ed. Springer, 2006.

[106] Normand Mousseau and G. T. Barkema. "Fast bond-transposition algorithms for generating covalent amorphous structures". In: *Curr. Opin. Solid State Mater. Sci.* 5 (2001), pp. 497–502.

[107] Masaharu Isobe. "Hard sphere simulation in statistical physics - methodologies and applications". In: *Mol. Simul.* 42.16 (2016), pp. 1317–1329.

[108] Etienne P Bernard, Werner Krauth, and David B Wilson. "Event-chain Monte Carlo algorithms for hard-sphere systems". In: *Phys. Rev. E* 80 (2009), p. 056704.

[109] Joshua A Anderson et al. "Massively parallel Monte Carlo for many-particle simulations on GPUs". In: *J. Comput. Phys.* 254 (2013), pp. 27–38.

[110] Masaharu Isobe and Werner Krauth. "Hard-sphere melting and crystallization with event-chain Monte Carlo". In: *J. Chem. Phys.* 143 (2015), p. 084509.

[111] B Widom. "Random Sequential Addition of Hard Spheres to a Volume". In: *J Chem Phys* 44 (1966), p. 3888.

[112] T S Grigera and G Parisi. "Fast Monte Carlo algorithm for supercooled soft spheres". In: *Phys. Rev. E* 63 (2001), 045102(R).

[113] Andrea Ninarello, Ludovic Berthier, and Daniele Coslovich. "Models and Algorithms for the Next Generation of Glass Transition Studies". In: *Phys. Rev. X* 7 (2017), p. 021039.

[114] A Okabe, B Boots, and K Sugihara. *Spatial Tessellations: Concepts and Applications of Voronoi Diagrams.* Wiley, 1992.

[115] Anne Poupon. "Voronoi and Voronoi-related tessellations in studies of protein structure and interaction". In: *Curr. Opin. Struct. Biol.* 14 (2004), pp. 233–241.

[116] B. J. Gellatly and J. L. Finney. "Characterisation of Models of Multicomponent Amorphous Metals: the Radical Alternative to the Voronoi Polyhedron". In: *J. Non. Cryst. Solids* 50 (1982), pp. 313–329.

[117] F Aurenhammer. "Power diagrams: properties, algorithms and applications". In: *SIAM J Comput* 16.1 (1987), pp. 78–96.

[118] FM Richards. "The Interpretation of Protein Structures : Total Volume, Group Volume Distributions and Packing Density". In: *J Mol Biol* 82 (1974), pp. 1–14.

[119] B N Boots. "The Spatial Arrangement of Random Voronoi Polygons". In: *Comput. Geosci.* 9.3 (1983), pp. 351–365.

[120] Masaharu Tanemura. "Statistical Distributions of Poisson Voronoi Cells in Two and Three Dimensions". In: *Forma* 18 (2003), pp. 221–247.

[121] Chris H Rycroft. "VORO++ : A three-dimensional Voronoi cell library in C ++". In: *Chaos* 19 (2009), p. 041111.

[122] D. Löffler et al. "Growth and structure of crystalline silica sheet on Ru(0001)". In: *Phys. Rev. Lett.* 105 (2010), p. 146104.

[123] Leonid Lichtenstein, Markus Heyde, and Hans Joachim Freund. "Crystalline-vitreous interface in two dimensional silica". In: *Phys. Rev. Lett.* 109 (2012), p. 106101.

[124] Mahdi Sadjadi et al. "Refining glass structure in two dimensions". In: *Phys. Rev. B* 96 (2017), 201405(R).

[125] James F. Shackelford. "Triangle rafts - extended Zachariasen schematics for structure modeling". In: *J. Non. Cryst. Solids* 49 (1982), pp. 19–28.

[126] Christin Büchner et al. "Building block analysis of 2D amorphous networks reveals medium range correlation". In: *J. Non. Cryst. Solids* 435 (2016), pp. 40–47.

[127] Louis Theran et al. “Anchored boundary conditions for locally isostatic networks”. In: *Phys. Rev. E* 92 (2015), p. 053306.

[128] P. Tangney and S. Scandolo. “An ab initio parametrized interatomic force field for silica”. In: *J. Chem. Phys.* 117 (2002), pp. 8898–8904.

[129] I. Zsoldos and A. Szasz. “Appearance of collectivity in two-dimensional cellular structures”. In: *Comput. Mater. Sci.* 15 (1999), pp. 441–448.

[130] Mahdi Sadjadi and M. F. Thorpe. “Ring correlations in random networks”. In: *Phys. Rev. E* 94 (2016), p. 062304.

[131] S R Broadbent and J M Hammersley. “Percolation processes I. Crystals and Mazes”. In: *Proc. Camb. Phil. Soc.Phil. Soc.* 53 (1956), pp. 629–641.

[132] Duncan S Callaway et al. “Network Robustness and Fragility : Percolation on Random Graphs”. In: *Phys. Rev. Lett.* 85.25 (2000), p. 5468.

[133] Dietrich Stauffer and Amnon Aharony. *Introduction to percolation theory.* 2nd ed. 2014.

[134] M F Sykes and J W Essam. “Exact Critical Percolation Probabilities for Site and Bond Problems in Two Dimensions”. In: *J. Math. Phys.* 5.8 (1964), p. 1117.

[135] Scott Kirkpatrick. “Percolation and Conduction”. In: *Rev. Mod. Phys.* 45.4 (1973), p. 574.

[136] H L Frisch, J M Hammersley, and D J A Welsh. “Monte Carlo Estimates of Percolation Probabilities for Various Lattices”. In: *Phys. Rev.* 126.3 (1962), pp. 949–951.

[137] B Y P Dean and N F Bird. “Monte Carlo estimates of critical percolation probabilities”. In: *Proc. Camb. Phil. Soc.* 63 (1967), p. 477.

[138] M E J Newman. “Mixing patterns in networks”. In: *Phys. Rev. E* 67 (2003), p. 026126.

[139] Di Zhou et al. “Assortativity decreases the robustness of interdependent networks”. In: *Phys. Rev. E* 86 (2012), p. 066103.

[140] C Schmeltzer et al. “Percolation of spatially constrained Erdos-Renyi networks with degree correlations”. In: *Phys. Rev. E* 89 (2014), p. 012116.

[141] V Kapko, D A Drabold, and M F Thorpe. “Electronic structure of a realistic model of amorphous graphene”. In: *Phys. Status Solidi* 247.5 (2010), pp. 1197–1200.

[142] Taishan Zhu and Elif Ertekin. “Phonons, Localization, and Thermal Conductivity of Diamond Nanothreads and Amorphous Graphene”. In: *Nano Lett.* 16 (2016), pp. 4763–4772.

[143] Franz Bamer, Firaz Ebrahem, and Bernd Markert. “Elementary plastic events in a Zachariasen glass under shear and pressure”. In: *Materialia* 9 (2020), p. 100556.

[144] Firaz Ebrahem, Franz Bamer, and Bernd Markert. “Vitreous 2D silica under tension : From brittle to ductile behaviour”. In: *Mater. Sci. Eng. A* 780 (2020), p. 139189.

[145] Oliver Whitaker. “Modelling of complex ring networks in two- and three-dimensions”. PhD thesis. University of Oxford, 2019.

[146] Xiaolei Ma, Janna Lowensohn, and Justin C Burton. "Universal scaling of polygonal desiccation crack patterns". In: *Phys. Rev. E* 99 (2019), p. 012802.

[147] Hisao Honda. "Description of cellular patterns by Dirichlet domains: The two-dimensional case". In: *J. Theor. Biol.* 72 (1978), pp. 523–543.

[148] Ross Carter et al. "Pavement cells and the topology puzzle". In: *Development* 144 (2017), pp. 4386–4397.

[149] Sangwoo Kim et al. "Hexagonal Patterning of the Insect Compound Eye : Facet Area Variatio , Defects, and Disorder". In: *Biophys. J.* 111 (2016), pp. 2735–2746.

[150] C. J. Lambert and D. L. Weaire. "Theory of the arrangement of cells in a network". In: *Metallography* 14.4 (1981), pp. 307–318.

[151] Susmit Kumar, Stewart K. Kurtz, and Denis Weaire. "Average number of sides for the neighbours in a Poisson-Voronoi tesselation". In: *Philos. Mag. B* 69.3 (1994), pp. 431–435.

[152] M. Blanc and A. Mocellin. "Grain coordination in plane sections of polycrystals". In: *Acta Metall.* 27 (1979), pp. 1231–1237.

[153] N. Rivier. "Statistical crystallography structure of random cellular networks". In: *Philos. Mag. B* 52.3 (1985), pp. 795–819.

[154] Michael A. Peshkin, Katherine J. Strandburg, and Nicolas Rivier. "Entropic predictions for cellular networks". In: *Phys. Rev. Lett.* 67.13 (1991), pp. 1803–1806.

[155] S N Chiu. "Mean-Value Formulae for the Neighbourhood of the Typical Cell of a Random Tessellation". In: *Adv. Appl. Probab.* 26 (1994), pp. 565–576.

[156] J K Mason, R Ehrenborg, and E A Lazar. "A geometric formulation of the law of Aboav – Weaire in two and three dimensions". In: *J. Phys. A* 45 (2012), p. 065001.

[157] H. J. Hilhorst. "Planar Voronoi cells: The violation of Aboav's law explained". In: *J. Phys. A* 39 (2006), pp. 7227–7243.

[158] M. E.J. Newman. "Assortative Mixing in Networks". In: *Phys. Rev. Lett.* 89.20 (2002), pp. 1–4.

[159] Rogier Noldus and Piet Van Mieghem. "Assortativity in complex networks". In: *J. Complex Networks* 3 (2015), pp. 507–542.

[160] Alexandros Chremos and Philip J. Camp. "Neighbor network in a polydisperse hard-disk fluid: Degree distribution and assortativity". In: *Phys. Rev. E* 76 (2007), p. 056108.

[161] Nelly Litvak and Remco van der Hofstad. "Uncovering disassortativity in large scale-free networks". In: *Phys. Rev. E* 87 (2013), p. 022801.

[162] J M Greneche and J M D Coey. "The topologically-disordered square lattice". In: *J. Phys. Fr.* 51 (1990), pp. 231–242.

[163] Franz R Eder et al. "A journey from order to disorder - atom by atom transformation from graphene to a 2D carbon glass". In: *Sci. Rep.* 4 (2014), p. 4060.

[164] Ordnance Survey. *Boundary-Line Data © Crown copyright and database right 2018.* 2018.

[165] Federal Office of Topography. *swissBOUNDARIES3D*. 2019.

[166] Eurostat. *NUTS Geodata © EuroGeographics for the administrative boundaries*. 2016.

[167] Etienne P Bernard and Werner Krauth. "Two-Step Melting in Two Dimensions : First-Order Liquid-Hexatic Transition". In: *Phys. Rev. Lett.* 107 (2011), p. 155704.

[168] Andrew H Marcus and Stuart A Rice. "Phase transitions in a confined quasi-two-dimensional colloid suspension". In: *Phys. Rev. E* 55.1 (1997), p. 637.

[169] Han-Rui Tian et al. "An Unconventional Hydrofullerene C66H4 with Symmetric Heptagons Retrieved in Low-Pressure Combustion". In: *J. Am. Chem. Soc.* 141 (2019), pp. 6651–6657.

[170] Runnan Guan et al. "Stable C92(26) and C92(38) as Well as Unstable C92(50) and C92(23) Isolated-Pentagon-Rule Isomers As Revealed by Chlorination of C92 Fullerene". In: *Inorg. Chem.* 58 (2019), pp. 5393–5396.

[171] Victor A Brotsman, Daria V Ignateva, and Sergey I Troyanov. "Chlorination-promoted Transformation of Isolated Pentagon Rule C78 into Fused-pentagons- and Heptagons-containing Fullerenes". In: *Chem Asian J* 12 (2017), pp. 2379–2382.

[172] Victor A Brotsman et al. "Rebuilding C60 : Chlorination-Promoted Transformations of the Buckminsterfullerene into Pentagon-Fused C60 Derivatives". In: *Inorg. Chem.* 57 (2018), pp. 8325–8331.

[173] Daishi Fujita et al. "Self-assembly of tetravalent Goldberg polyhedra from 144 small components". In: *Nature* 540 (2016), pp. 563–566.

[174] Zhi Wang et al. "Assembly of silver Trigons into a buckyball-like Ag180 nanocage". In: *PNAS* 114.46 (2017), pp. 12132–12137.

[175] A E Roth, C D Jones, and D J Durian. "Coarsening of a two-dimensional foam on a dome". In: *Phys. Rev. E* 86 (2012), p. 021402.

[176] P N Pusey and W Van Megen. "Phase behaviour of concentrated suspensions of nearly hard colloidal spheres". In: *Nature* 320 (1986), p. 340.

[177] Alice L Thorneywork et al. "Radial distribution functions in a two-dimensional binary colloidal hard sphere system". In: *J. Chem. Phys.* 140 (2014), p. 161106.

[178] Alice L Thorneywork et al. "Structure factors in a two-dimensional binary colloidal hard sphere system". In: *Mol. Phys.* 116 (2018), pp. 3245–3257.

[179] R Roth, R Evans, and A A Louis. "Theory of asymmetric nonadditive binary hard-sphere mixtures". In: *Phys. Rev. E* 64 (2001), p. 051202.

[180] R Y Yang, R P Zou, and A B Yu. "Voronoi tessellation of the packing of fine uniform spheres". In: *Phys. Rev. E* 65 (2002), 041302 Voronoi.

[181] VS Kumar and V Kumaran. "Voronoi neighbor statistics of hard-disks and hard-spheres". In: *J Chem Phys* 123 (2005), p. 074502.

[182] A Jaster. "Computer simulations of the two-dimensional melting transition using hard disks". In: *Phys. Rev. E* 59.3 (1999), pp. 2594–2602.

[183] Sander Pronk and Daan Frenkel. "Melting of polydisperse hard disks". In: *Phys. Rev. E* 69 (2004), p. 066123.

[184] Sebastian C Kapfer and Werner Krauth. "Two-Dimensional Melting : From Liquid-Hexatic Coexistence to Continuous Transitions". In: *Phys. Rev. Lett.* 114 (2015), p. 035702.

[185] Alice L Thorneywork. "Structure and dynamics of two-dimensional colloidal hard spheres". PhD thesis. University of Oxford, 2015.

[186] Q Weikai, A P Gantapara, and Marjolein Dijkstra. "Two-stage melting induced by dislocations and grain boundaries in monolayers of hard spheres". In: *Soft Matter* 10.30 (2014), p. 5449.

[187] Y Peng et al. "Short-time self-diffusion of nearly hard spheres at an oil–water interface". In: *J Fluid Mech* 618 (2009), pp. 243–261.

[188] N Vogel et al. "Direct visualization of the interfacial position of colloidal particles and their assemblies†". In: *Nanoscale* 6 (2014), pp. 6879–6885.

[189] Elisa Tamborini, C Patrick Royall, and Pietro Cicuta. "Correlation between crystalline order and vitrification in colloidal monolayers". In: *J. Phys. Condens. Matter* 27 (2015), p. 194124.

[190] H Imai, I Masao, and K Murota. "Voronoi Diagram in the Laguerre Geometry and its Applications". In: *SIAM J* 14.1 (1985), pp. 93–105.

[191] N Rivier. "Geometry and Fluctuations of Surfaces". In: *J. Phys. Colloq.* 51 (1990), pp. 309–317.

[192] P Bhattacharyya and B K Chakrabarti. "The mean distance to the nth neighbour in a uniform distribution of random points: an application of probability theory". In: *Eur. J. Phys.* 29 (2008), p. 639.

[193] L Oger et al. "Comparison of two representations of a random cut of identical sphere packing". In: *Eur. Phys. J. B* 14 (2000), pp. 403–406.

[194] Annie Gervois, Luc Oger, and Jean-Paul Troadec. "Random cuts in binary mixtures of spheres". In: *Phys. Rev. E* 70 (2004), p. 031112.

[195] U Hahn and U Lorz. "Stereological analysis of the spatial Poisson-Voronoi tessellation". In: *J. Microsc.* 175.3 (1994), pp. 176–185.

[196] Simone Falco et al. "Generation of 3D polycrystalline microstructures with a conditioned Laguerre-Voronoi tessellation technique". In: *Comput. Mater. Sci.* 136 (2017), pp. 20–28.

[197] Dorian Depriester and Régis Kubler. "Radical Voronoï tessellation from random pack of polydisperse spheres Prediction of the cells' size distribution". In: *Comput. Des.* 107 (2019), pp. 37–49.

[198] Matthew O Blunt et al. "Random Tiling and Topological Defects in a Two-Dimensional Molecular Network". In: *Science (80-.).* 322 (2008), pp. 1077–1081.

[199] P W Anderson. "RESONATING VALENCE BONDS" A NEW KIND OF INSULATOR?" In: *Mat. Res. Bull.* 8 (1973), pp. 153–160.

[200] Philip J Camp, Amparo Fuertes, and J P Attfield. "Subextensive Entropies and Open Order in Perovskite Oxynitrides". In: *J Am Chem Soc* 134 (2012), pp. 6762–6766.

[201] R Comes, M Lambert, and A Guinier. "THE CHAIN STHUCTURE OF BaT1O3 AND KNbO3". In: *Solid State Commun.* 6 (1968), pp. 715–719.

[202] G Algara-Siller et al. "Square ice in graphene nanocapillaries". In: *Nature* 519 (2015), p. 443.

[203] YinBo Zhu, FengChao Wang, and HengAn Wu. "Structural and dynamic characteristics in monolayer square ice". In: *J. Chem. Phys.* 147 (2017), p. 044706.

[204] Simon J Hibble et al. "Structures of Pd (CN)2 and Pt (CN)2: Intrinsically Nanocrystalline Materials?" In: *Inorg. Chem.* 50 (2011), pp. 104–113.

[205] Qing-Na Zheng et al. "Adaptive Reorganization of 2D Molecular Nanoporous Network Induced by Coadsorbed Guest Molecule". In: *Langmuir* 30 (2014), pp. 3034–3040.

[206] Lars Postulka et al. "Spin Frustration in an Organic Radical Ion Salt Based on a Kagome-Coupled Chain Structure". In: *J. Am. Chem. Soc.* 138 (2016), pp. 10738–10741.

[207] Ting Chen et al. "2D Hexagonal Tilings Based on Triangular and Hexagonal Structural Units in the Self-Assembly of Thiacalix[4]arene Tetrasulfonate on an Au(111) Surface". In: *Chem Asian J* 6 (2011), pp. 1811–1816.

[208] Austin D Griffith and Robert S Hoy. "Densest versus jammed packings of two-dimensional bent-core trimers". In: *Phys. Rev. E* 98 (2018), p. 042910.

[209] Jose I Urgel et al. "Five-Vertex Lanthanide Coordination on Surfaces: A Route to Sophisticated Nanoarchitectures and Tessellations". In: *J Phys Chem C* 118 (2014), pp. 12908–12915.

[210] N P Kryuchkov et al. "Complex crystalline structures in a two-dimensional core-softened system". In: *Soft Matter* 14 (2018), p. 2152.

[211] Bai-Qiao Song et al. "Periodic tiling of triangular and square nanotubes in a cationic metal – organic framework for selective anion exchange †". In: *Chem Commun* 51 (2015), pp. 9515–9518.

[212] William D Piñeros, Michael Baldea, and Thomas M Truskett. "Designing convex repulsive pair potentials that favor assembly of kagome and snub square lattices". In: *J. Chem. Phys.* 145 (2016), p. 054901.

[213] Mia Baise et al. "Negative Hydration Expansion in ZrW2O8 : Microscopic Mechanism, Spaghetti Dynamics, and Negative Thermal Expansion". In: *Phys. Rev. Lett.* 120 (2018), p. 265501.

[214] V A Gorbunov, S S Akimenko, and A V Myshlyavtsev. "Cross-impact of surface and interaction anisotropy in the self-assembly of organic adsorption monolayers : a Monte Carlo". In: *Phys Chem Chem Phys* 19 (2017), pp. 17111–17120.

[215] Damien Nieckarz, Wojciech Rzysko, and Paweł Szabelski. "On-surface self-assembly of tetratopic molecular building blocks". In: *Phys Chem Chem Phys* 20 (2018), p. 23363.

[216] C Buzano et al. "Two-dimensional lattice-fluid model with waterlike anomalies". In: *Phys. Rev. E* 69 (2004), p. 061502.

[217] Philip J Camp. "Structure and phase behavior of a two-dimensional system with core-softened and long-range repulsive interactions". In: *Phys. Rev. E* 68 (2003), p. 061506.

[218] Michael Griebel and Jan Hamaekers. "Molecular dynamics simulations of boron-nitride nanotubes embedded in amorphous Si-B-N". In: *Comput. Mater. Sci.* 39 (2007), pp. 502–517.

[219] Arkadiy Simonov et al. "Hidden diversity of vacancy networks in Prussian blue analogues". In: *Nature* 578 (2020), p. 256.

[220] Marian Florescu, Salvatore Torquato, and Paul J Steinhardt. "Designer disordered materials with large, complete photonic band gaps". In: *PNAS* 106.49 (2009), pp. 20658–20663.

[221] Steven R Sellers et al. "Local self-uniformity in photonic networks". In: *Nat. Commun.* 8 (2017), p. 14439.

[222] Larry Wasserman. "Topological Data Analysis". In: *Annu. Rev. Stat. Appl.* 5 (2018), p. 501.

[223] Herbert Edelsbrunner and John Harer. "Persistent homology - a survey". In: *Contemp. Math.* 453 (2008), p. 257.

[224] Benjamin M G D Carter et al. "Structural covariance in the hard sphere fluid". In: *J. Chem. Phys.* 148 (2018), p. 204511.

[225] Fei Jiang, Takeshi Tsuji, and Tomoyuki Shirai. "Pore Geometry Characterization by Persistent Homology Theory". In: *Water Resour. Res.* 54 (2018), pp. 4150–4163.

[226] Lee Steinberg, John Russo, and Jeremy Frey. "A new topological descriptor for water network structure". In: *J. Cheminform.* 11.48 (2019), pp. 1–11.

[227] Kelin Xia et al. "Persistent Homology for the Quantitative Prediction of Fullerene Stability". In: *J. Comput. Chem.* 36 (2015), pp. 408–422.

[228] Yasuaki Hiraoka et al. "Hierarchical structures of amorphous solids characterized by persistent homology". In: *PNAS* 113.26 (2016), pp. 7035–7040.

[229] Yohei Onodera et al. "Understanding diffraction patterns of glassy, liquid and amorphous materials via persistent homology analyses". In: *J. Ceram. Soc. Japan* 127.12 (2019), pp. 853–863.

[230] Takenobu Nakamura et al. "Persistent homology and many-body atomic structure for medium-range order in the glass". In: *Nanotechnology* 26 (2015), p. 304001.

[231] Abraham Gutierrez, Mickaël Buchet, and Sylvain Clair. "Persistent Homology To Quantify the Quality of Surface- Supported Covalent Networks". In: *ChemPhysChem* 20 (2019), pp. 1–7.

[232] The GUDHI Project. *GUDHI User and Reference Manual.* 3.2.0. GUDHI Editorial Board, 2020.

[233] Ulderico Fugacci et al. "Persistent homology: a step-by-step introduction for newcomers". In: *Smart Tools Apps Comput. Graph.* October (2016).

[234] Nina Otter et al. "A roadmap for the computation of persistent homology". In: *EPJ Data Sci.* 6 (2017), p. 1.

[235] Afra Zomorodian and Gunnar Carlsson. “Computing Persistent Homology”. In: *Discret. Comput Geom* 33 (2005), pp. 249–274.